J. Fluid Mech. (2020), *vol*. 899, A18. © The Author(s), 2020.
Published by Cambridge University Press
doi:10.1017/jfm.2020.462

Onset of Darcy–Bénard convection in a horizontal layer of dual-permeability medium with isothermal boundaries

Andrey Afanasyev†

Institute of Mechanics, Moscow State University, Moscow 119192, Russia

(Received 26 December 2019; revised 9 April 2020; accepted 4 June 2020)

The onset of natural convection in an infinite horizontal layer of a fractured-porous medium is investigated. The breakdown of local equilibrium between the low-permeability matrix and fractures embedded in the matrix is accounted for by applying the dual-porosity dual-permeability model. The symmetric case of impermeable and isothermal boundaries of the layer is examined in detail. By means of linear perturbation analysis, the dispersion equation is derived, and its solutions are investigated numerically as well as analytically in a few asymptotic cases. It is determined that the critical Rayleigh number depends only on the permeability, heat conductivity ratios and the coefficient of heat and mass transfer between fractures and matrix. It is shown that the convection exhibits a rich variety of flow patterns at near-critical conditions. Nine flow regimes can arise with co-rotating or counter-rotating convection cells in the fractures and matrix. These modes can bifurcate to the plane flow regime, in which only cross-medium convection occurs. The complete classification of the flow regimes is provided and plotted in a solution map. Finally, the theoretical analysis is supported by the numerical modelling of the convection by using a reservoir simulator.

Key words: convection in porous media

1. Introduction

Internal natural convection in a horizontal layer of a porous medium uniformly heated from below has been broadly investigated by many authors. The simplest case of convection in a homogeneous porous medium was first considered by Horton & Rogers (1945) and independently by Lapwood (1948), who determined the critical Rayleigh (Rayleigh–Darcy) number, $Ra_c = 4\pi^2$, in the case of the isothermal and impermeable boundaries of the layer. The analysis was extended to other boundary conditions by Nield (1968). Afterwards, this Horton–Rogers–Lapwood (HRL) problem was considered, accounting for additional physical processes, including convection in anisotropic media (Epherre 1975), non-Darcy flow (Walker & Homsy 1977), hydrodynamic dispersion of temperature (Kvernvold & Tyvand 1980), nonlinear effects (Rees, Magyari & Keller 2005), viscous dissipation (Magyari, Rees & Keller 2005) and other phenomena, which have been reviewed by Nield & Bejan (2017).

† Email address for correspondence: afanasyev@imec.msu.ru

Significant attention has been concentrated on convection in porous media considering local thermal non-equilibrium (LTNE), as reviewed by Straughan (2015). Darcy–Bénard convection was studied by Banu & Rees (2002) and Postelnicu & Rees (2003) for the case when the thermal equilibrium between the skeleton of the porous medium and the fluid breaks down, and these two solid and fluid phases have different temperatures. Using a two-temperature model, they showed that LTNE influences the onset of convection. A more general case of convection in bi-dispersed porous medium (BDPM) has received attention from Nield & Kuznetsov (2006) and Straughan (2009). The BDPM is a standard porous medium in which the solid phase is replaced with another porous medium (Chen, Cheng & Zhao 2000). Thus, there are macropores in the first medium and micropores in the second medium, which is nested in the first one. Both media have their own temperatures and fluid velocities. It was found that the critical Rayleigh number in BDPM can be much larger than that in the equivalent homogeneous porous medium. Recently, this study was extended by Straughan (2018, 2019) to the case of anisotropic BDPM.

Understanding and predicting convection in BDPM is of interest for microfluidic applications related to designing heat transfer and insulation in small devices (Straughan 2015), as well as for flows over much larger space scales in geophysical applications. For example, convection in naturally fractured rocks has implications for geothermal energy extraction (Gérard *et al.* 2006; Nie *et al.* 2012), ore deposits (Weis 2015; Afanasyev *et al.* 2018) and other transport processes in the Earth's crust (Simmons 2005). The dual-porosity dual-permeability model is a standard model for predicting fluid and heat transport in fractured rocks, although other approaches exist (Dietrich *et al.* 2005). As for BDPM, such a model is built on the double-continuum concept by assuming the existence of two nested porous media, namely, the fractures, corresponding to the macropores, and the lower-permeability matrix blocks between the fractures corresponding to the micropores (Barenblatt, Zheltov & Kochina 1960; Warren & Root 1963). The size of the matrix blocks can significantly exceed tens of metres in geologic reservoirs, which drastically increases the time required for pressure and temperature equilibration between the media. In many cases, natural flow in subsurface reservoirs is very slow. It can be simulated by employing Darcy's law, with the mass transfer between fractures and matrix driven by the difference in pressures, and the conduction heat transfer driven by the difference in temperatures (Pruess 1983; Pruess & Narasimhan 1985). Thus, the governing equations for BDPM differ from those for the dual-porosity dual-permeability medium (DPM). The BDPM model usually accounts for the Brinkman term and momentum transfer between the media and neglects the fluid transport associated with different pressures in the fractures and the matrix. On the contrary, the DPM model accounts for the latter but assumes Darcy flow without accounting explicitly for the momentum transfer. Thus, the existing works on convection in BDPM cannot be directly applied to hydrothermal systems composed of naturally fractured rocks.

Hydrothermal fluid circulation through naturally fractured rocks exhibits a rich variety of flow patterns that have been widely investigated by means of the numerical modelling of Darcy flow. Yang, Latychev & Edwards (1998) and Diersch & Kolditz (2002) showed that convection patterns in fractured-porous media differ from those in homogeneous media because fractures represent preferential pathways for fluid flow. The flow patterns of free convection were investigated by Simmons, Sharp & Nield (2008). It was shown that there can arise both intra-fracture convection patterns, i.e. when convection cells are parallel to fracture planes, and inter-fracture patterns, when convection cells are perpendicular to the fracture plane. Every convection cell is located in a single fracture in the case of intra-fracture patterns, whereas the cells are stretched over a pair of fractures in the case of inter-fracture patterns. Simmons *et al.* (2008) stress that both these modes must be

taken into account to avoid underestimating the likelihood of convection. Recently, these and other patterns were simulated by Vujević *et al.* (2014) and Vujević & Graf (2015). They considered different types of fracture networks and investigated how the network parameters influence the onset of convection and the flow patterns. It was found that the existence of regular fracture circuits lead to the onset of inter-fracture convection. Also, counter-rotating circulation cells can develop in nearby fractures.

The theoretical analysis, which to some extent can be applied for estimating the critical Rayleigh number in DPM, was conducted by McKibbin & O'Sullivan (1980). They considered the Darcy–Bénard convection in the case of a layered porous medium when particular layers, which are thin and characterized by high permeability, are considered fractures (McKibbin & Tyvand 1984). The study by Banu & Rees (2002) can be applied to the convection in a dual-porosity (not dual-permeability) medium when the flow occurs only through fractures. To date, there has been no theoretical analysis of convection patterns in DPM, particularly in the case of dual permeability when fluid flow through each of the media and between them is possible. In addition to the noted practical significance, such an analysis would be useful for the better classification of the flow regimes simulated by Vujević *et al.* (2014) and others.

In this theoretical study, we analyse the flow patterns in the fractured-porous medium by considering the HRL problem for DPM. We examine the symmetric case of isothermal upper and lower boundaries of the layer when the respective spectral problem admits a relatively simple analytical solution and leave the cases of other boundary conditions for later studies. We investigate the critical Rayleigh number dependence upon similarity parameters and support analytical findings with numerical modelling of the convection flow. With a certain degree of approximation, the considered problem can be applied for understanding convective flows in a horizontal layer of a hydrothermal system bounded from above and below with impermeable rocks. We investigate the parameters leading to the onset of convection in such a layer and show that nine flow regimes can be established, depending on the parameters of the layer.

2. Problem statement

Let us consider an infinite horizontal layer of DPM of height H saturated with a single-phase fluid (figure 1, $x, y \in (-\infty, \infty)$). Both the lower and upper boundaries of the layer are impermeable and isothermal, i.e. constant temperatures T_+ and $T_- = 0$ are held at $z = 0$ and $z = H$, respectively. It is assumed that the layer is uniformly heated from below, and so, $T_+ > T_-$.

Applying the multi-continuum approach, we model convection in the fractured-porous medium using two inter-penetrating porous media (figure 1). The first medium, Φ^f, corresponds to fractures, fissures or channels, forming high-permeability pathways for fluid, whereas the second medium, Φ^m, corresponds to low-permeability matrix blocks between the fractures. In what follows, we denote the parameters of fractures and matrix with the superscripts f and m, respectively. Furthermore, we will not refer to Φ^f and Φ^m as 'fractures' and 'matrix' because the study may include a wider range of applications in which Φ^f and Φ^m correspond to different types of pore space.

We characterize the pore space of DPM with the relative volume $\gamma = V^f/V$ of the medium Φ^f, where $V = V^f + V^m$ is the bulk representative elementary volume of DPM, and $V^j, j = f, m$ is the elementary volume occupied by Φ^j. Then, the relative volume of the medium Φ^m is $1 - \gamma = V^m/V$. We characterize each medium with its own porosity, $\phi^j = V^j_{por}/V^j$, and absolute permeability, K^j, where V^j_{por} is the volume of pore space in

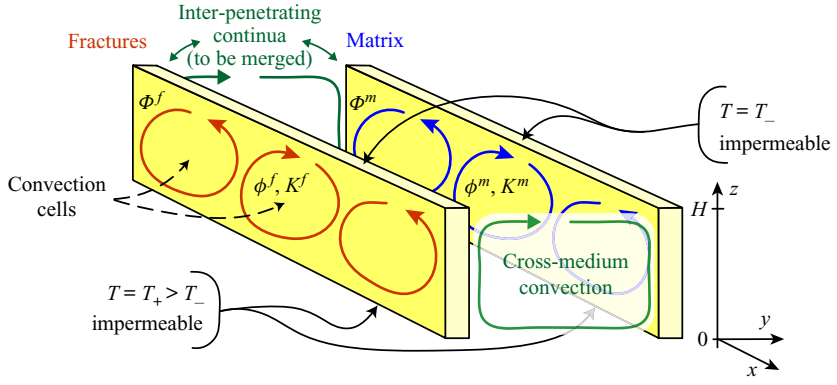

FIGURE 1. Sketch of the horizontal layer of DPM, which is modelled with two inter-penetrating continua Φ^f and Φ^m. For clarity, the layers corresponding to each continuum are drawn separately.

the corresponding medium. Then, the pore spaces of Φ^f and Φ^m occupy the fractions $\gamma\phi^f$ and $(1-\gamma)\phi^m$ of the elementary volume V.

For the mathematical modelling of the natural convection, we formulate for each medium its own Darcy's law, along with the mass and energy balance equations. Furthermore, we investigate convection in the Oberbeck–Boussinesq approximation, and we thus account for the fluid density changes only in the terms containing the gravity acceleration $\boldsymbol{g}$. The system of governing equations, which can be derived from Pruess (1983), Pruess & Narasimhan (1985) and Dietrich *et al.* (2005), consists of

$$\rho^j = \rho_0(1-\beta T^j), \quad j = f, m, \tag{2.1}$$

$$\boldsymbol{u}^j = -\frac{K^j}{\mu}(\nabla p^j - \rho^j \boldsymbol{g}), \tag{2.2}$$

$$\nabla \cdot \boldsymbol{u}^j = -b^j q^{fm}, \quad q^{fm} = \sigma_1 \frac{K^m}{\mu}(p^f - p^m), \tag{2.3a,b}$$

$$\begin{aligned}(\rho c)^j \partial_t T^j + \nabla \cdot (\rho_0 c T^j \boldsymbol{u}^j) + \nabla \cdot (p^j \boldsymbol{u}^j) \\ = \rho^j \boldsymbol{g} \cdot \boldsymbol{u}^j + \lambda^j \nabla^2 T^j - b^j q^{fm}(\rho_0 c T^{fm} + p^j) - b^j \sigma_2 \lambda^m (T^f - T^m),\end{aligned} \tag{2.4}$$

where ρ, μ and $\beta = \text{const}$ are the fluid density, the dynamic viscosity and the thermal expansion coefficient, respectively; ρ_0 is the reference value of the fluid density; $\boldsymbol{u}$ is the Darcy velocity; p is the pressure; T is the temperature; q^{fm} is the mass flux from Φ^f into Φ^m; $b^f = 1$ and $b^m = -1$ are constants; λ^j is the bulk heat conductivity of saturated medium Φ^j; and $(\rho c)^j$ is the bulk volume heat capacity of Φ^j, expressed as

$$(\rho c)^f = \gamma(\phi^f \rho_0 c + (1-\phi^f)\rho_r c_r), \quad (\rho c)^m = (1-\gamma)(\phi^m \rho_0 c + (1-\phi^m)\rho_r c_r).$$

Here, the subscript r denotes the parameters of the solid phase, which are assumed to be equal in both media, and c and c_r are the specific heat capacities of the fluid and solid phase, respectively.

Equation (2.1) is the fluid equation of state, (2.2) is Darcy's law and (2.3a) and (2.4) are the mass and energy balance equations for each medium. In (2.4), the terms $\nabla \cdot (p^j \boldsymbol{u}^j)$ and $q^{fm}(p^f - p^m)$, obtained by summing (2.4) for $j = f$ and m, correspond to the work of

pressure when the fluid flows through each medium and between the media, respectively (Brownell, Garg & Pritchett 1977; Garg & Pritchett 1977); the term $\rho^j \boldsymbol{g}\cdot\boldsymbol{u}^j$ is the work of gravity; $\lambda^j\nabla^2 T^j$ corresponds to conductive heat transfer through each medium; and $q^{fm}\rho_0 c T^{fm}$ and $\sigma_2\lambda^m(T^f - T^m)$ are the convective and conductive heat transfers from Φ^f to Φ^m. Here, T^{fm} is the upwind value of temperature. If the fluid flows from Φ^f into Φ^m ($q^{fm} > 0$), then $T^{fm} = T^f$, or *vice versa*; if it flows from Φ^m into Φ^f ($q^{fm} < 0$), then $T^{fm} = T^m$. The definition of T^{fm} is irrelevant in the linear perturbation analysis carried out in §§ 4–7 but is used in the numerical modelling of fluid transport presented in § 8. For further clarification of the energy balance equation, we substitute (2.2) and (2.3*a*) into (2.4) thereby expressing it as

$$\begin{aligned}&(\rho c)^j\partial_t T^j + \rho_0 c\boldsymbol{u}^j\cdot\nabla T^j - \lambda^j\nabla^2 T^j\\ &\quad= \mu(\boldsymbol{u}^j)^2/K^j - b^j\rho_0 c q^{fm}(T^{fm} - T^j) - b^j\sigma_2\lambda^m(T^f - T^m).\end{aligned}\tag{2.5}$$

Thus, the energy balance equation for each Φ^j is the usual advection–diffusion equation for temperature with a source term – i.e. the right-hand side of (2.5) – equal to the sum of a dissipation term $\mu(\boldsymbol{u}^j)^2/K^j$ (Ene & Sanchez-Palencia 1982) and the convective and conductive heat fluxes between Φ^j. The quadratic term $\mu(\boldsymbol{u}^j)^2/K^j$ is the consequence of including the works of pressure and gravity in the energy balance (2.4). If one of the works is neglected and the other one is taken into account, then the dissipation term is not quadratic, and the dissipation can become negative. The governing equations thus contradict the second law of thermodynamics (Afanas'ev 2012). Therefore, both works must be either taken into account or neglected. For generality of this study, we include both works in (2.4).

The mass flux and the conductive heat flux between the media, q^{fm} and $\sigma_2\lambda^m(T^f - T^m)$, respectively, are proportional to the products $\sigma_1 K^m/\mu$ and $\sigma_2\lambda^m$, which are the coefficients of mass and heat transfer between Φ^j. Here, σ_1 and σ_2 are the shape factors characterizing the fracture network. The constants σ_1 and σ_2 can be derived under the assumption of either quasi-steady (Warren & Root 1963; Kazemi *et al.* 1976) or transient (Pruess & Narasimhan 1985; Lim & Aziz 1995) exchange between Φ^j. Independently of the exchange model, we further consider σ_1 and σ_2 as given parameters. The transfer coefficients $\sigma_1 K^m/\mu$ and $\sigma_2\lambda^m$ are proportional to K^m and λ^m, reflecting that the mass and heat exchange between Φ^j is mostly defined by the permeability and heat conductivity in Φ^m. In applications, σ_1 cannot be equal to σ_2. For example, σ_1 can be reduced by solute precipitation on the fracture walls and associated local permeability reduction. Similarly, in microfluidic applications, σ_2 can be reduced by designing DPM with insulated layers on the boundaries of high-permeability channels. However, in §§ 6–8, for simplicity, we restrict the study to the case of

$$\sigma_1 \equiv \sigma_2.\tag{2.6}$$

The bulk parameters of DPM are expressed as

$$\left.\begin{aligned}\overline{\phi} &= \gamma\phi^f + (1-\gamma)\phi^m, \quad \overline{K} = K^f + K^m,\\ \overline{(\rho c)} &= (\rho c)^f + (\rho c)^m, \quad \overline{\lambda} = \lambda^f + \lambda^m,\end{aligned}\right\}\tag{2.7}$$

where, and in what follows, the bar denotes bulk quantities. These are the parameters of the homogeneous porous medium (EPM), which is equivalent to DPM under local equilibrium, $p^f = p^m$ and $T^f = T^m$. If we sum (2.2)–(2.4) pairwise for $j = f$ and m and place $p^f = p^m$ and $T^f = T^m$, then we obtain the equations for transport in EPM with the bulk parameters (2.7).

We assume that the system is in the conduction state. Thus, the basic steady-state solution represents the hydrostatic fluid distribution under local equilibrium between Φ^j

$$T^j = T_+ - \alpha_0 z, \quad \boldsymbol{u}^j = 0, \tag{2.8a,b}$$

where $\alpha_0 = (T_+ - T_-)/H > 0$ is constant. In the state (2.8), the porous medium is saturated with quiescent thermally stratified fluid.

The basic solution (2.8) satisfies the following boundary conditions:

$$\left.\begin{aligned} T^j = T_+, \quad u_z^j = 0 \quad \text{on } z = 0, \\ T^j = T_-, \quad u_z^j = 0 \quad \text{on } z = H, \end{aligned}\right\} \tag{2.9}$$

corresponding to the isothermal and impermeable lower and upper boundaries of the layer. Here, u_z is the vertical component of fluid velocity.

3. Governing equations in dimensionless form

We take the layer thickness H as the characteristic length scale and denote the characteristic scales of the other parameters by the subscript s

$$\rho_s = \rho_0 \alpha_0 \beta H, \quad p_s = \rho_s g H, \quad u_s = \frac{\overline{K}}{\mu}\rho_s g,$$

$$t_s = \frac{H\overline{\phi}}{u_s} = \frac{H\overline{\phi}\mu}{\overline{K}\rho_s g}, \quad T_s = T_+ - T_- = \alpha_0 H.$$

According to (2.1) and (2.8*a*), the density scale ρ_s is the fluid density change across the layer in the steady-state solution (2.8). Thus, the pressure scale p_s is the increase in hydrostatic pressure head of height H if the temperature at each point of the layer decreases by T_s. The scale u_s is the instant Darcy velocity of a representative elementary volume of fluid heated up to the temperature T_+ and placed in the equivalent homogeneous layer of uniform temperature T_-, and t_s is the time required for this volume to float up across the layer, assuming no heat exchange between the volume and the solid phase or other fluid.

Using the characteristic scales, we introduce the dimensionless parameters as

$$\boldsymbol{r}_* = \frac{\boldsymbol{r}}{H}, \quad \upsilon_* = \frac{\upsilon}{\upsilon_s}, \quad \boldsymbol{r} = (x, y, z), \quad \upsilon = (\rho, p, T, u, t), \tag{3.1}$$

where the asterisks denote the dimensionless variables, and $\boldsymbol{r}$ is the position vector.

After substituting (2.7) and (3.1) into (2.1)–(2.4) and further omitting the asterisks of the dimensionless parameters, we obtain

$$\left.\begin{aligned} \rho^j = \alpha^{-1} - T^j, \quad \boldsymbol{u}^j = -\kappa^j(\nabla p^j + \rho^j \boldsymbol{e}_z), \\ \boldsymbol{\nabla}\cdot\boldsymbol{u}^j = -b^j q^{fm}, \quad q^{fm} = \frac{\kappa^m}{B_1}(p^f - p^m), \\ S^j \partial_t T^j + \boldsymbol{u}^j\cdot\nabla T^j + \Upsilon \boldsymbol{u}^j\cdot\nabla p^j = -\Upsilon\rho^j \boldsymbol{u}^j\cdot\boldsymbol{e}_z + \frac{\kappa^j}{Ra^j}\nabla^2 T^j \\ -b^j q^{fm}(T^{fm} - T^j) - \frac{b^j \Lambda^m}{\overline{Ra}B_2}(T^f - T^m), \end{aligned}\right\} \tag{3.2}$$

where $\boldsymbol{e}_z$ is the unit vector in the opposite direction to gravity ($\boldsymbol{g} = -g\boldsymbol{e}_z$), and the following dimensionless quantities are introduced:

$$\left.\begin{aligned} &S^j = \frac{(\rho c)^j}{\overline{\phi}\rho_0 c}, \quad Ra^j = \frac{\rho_0^2 c K^j g H \alpha}{\lambda^j \mu}, \quad \overline{Ra} = \frac{\rho_0^2 c \overline{K} g H \alpha}{\overline{\lambda}\mu}, \quad \Upsilon = \frac{g\beta H}{c}, \\ &\alpha = \alpha_0 \beta H = \frac{\rho_s}{\rho_0}, \quad \kappa^j = \frac{K^j}{\overline{K}}, \quad \Lambda^j = \frac{\lambda^j}{\overline{\lambda}}, \quad B_i = \frac{1}{\sigma_i H^2}, \quad i = 1, 2. \end{aligned}\right\} \tag{3.3}$$

According to (3.3), the inequalities $S^j > 0$, $Ra^j > 0$, and $\overline{Ra} > 0$ hold, where Ra^j is the Rayleigh number for the medium Φ^j. The quantities S^j and Ra^j for Φ^j are related to $\overline{S}$ and $\overline{Ra}$ for EPM by

$$\overline{S} = S^f + S^m, \quad \frac{1}{\overline{Ra}} = \frac{\kappa^f}{Ra^f} + \frac{\kappa^m}{Ra^m}, \quad \overline{Ra} = \Lambda^f Ra^f + \Lambda^m Ra^m, \tag{3.4}$$

where, according to the definitions of κ^j, Λ^j, and Ra^j in (3.3), both expressions for $\overline{Ra}$ can be applied at the same time.

The ratios κ^j and Λ^j characterize the permeability and heat conductivity distribution between the two media, where $\kappa^f + \kappa^m = 1$ and $\Lambda^f + \Lambda^m = 1$. The fractions κ^f and Λ^f of the bulk quantities $\overline{K}$ and $\overline{\lambda}$ belong to Φ^f, whereas the fractions κ^m and Λ^m belong to Φ^m. The parameters K^j and λ^j can vary in a wide range, depending on the particular porous medium. For example, λ^j depends on the heat conductivities of the solid and fluid phases, as well as the topology of the pore space, which can lead to either parallel or series transmission of heat (Ghanbarian & Daigle 2016). The permeability K^j can also vary in a wide range depending on the topology of the pore space and the fracture density. The fracture permeability K^f can be both larger and less than K^m because it is proportional to the volumetric flux density $\boldsymbol{u}^f$ (Nield & Bejan 2017). The case of $K^f < K^m$ corresponds to $\gamma \ll 1$ when $|\boldsymbol{u}^f| < |\boldsymbol{u}^m|$ even though the intrinsic average velocity in Φ^f can be larger than that in Φ^m, i.e. $|\boldsymbol{u}^f|/\gamma\phi^f > |\boldsymbol{u}^m|/(1-\gamma)\phi^m$. To account for all types of porous medium, we assume $0 \le \kappa^j \le 1$ and $0 \le \Lambda^j \le 1$.

The quantities B_i characterize the intensity of mass and heat transfer between Φ^j. If $B_i \ll 1$, then the flow occurs under local equilibrium and one can use EPM as a substitute for DPM. If $B_i \sim 1$ or $B_i \gg 1$, then the local equilibrium breaks down and one must apply DPM in order to account for different pressures and temperatures in Φ^j. In geophysical applications, the shape factors σ_i can be estimated as $\sigma_i = d/L_b^2$, where L_b is the characteristic distance between fractures, and typically, the constant d lies in the range of 4–27 (Kazemi *et al.* 1976; Lim & Aziz 1995). The double-continuum concept is meaningful if $L_b \ll H$, i.e. if a representative elementary volume in Φ^f can be defined for volume averaging (Dietrich *et al.* 2005). The relation $L_b \ll H$ is equivalent to $B_i \ll 1$. As noted above, particular physical phenomena, e.g. local permeability reduction due to solute precipitation, can increase B_i, but we bear in mind that $B_i > 1$ is unlikely in a geophysical context. In a designed porous medium, e.g. if Φ^f corresponds to channels embedded into a low-permeability medium, the meaningful values of B_i can be higher than 1. For convection in BDPM, Nield & Kuznetsov (2006) consider B_2 in the range of 0–100. Further, we investigate convection regimes at $0 \le B_i \le 100$, $0 \le \kappa^j \le 1$, and $0 \le \Lambda^j \le 1$ so as not to miss any application.

Substituting (2.1) and (2.2) into (2.8*b*) and integrating the obtained equation, we reduce (2.8) and (2.9) to the following dimensionless form:

$$p^j = 1 - \frac{1-\alpha}{\alpha} z - \frac{z^2}{2}, \quad T^j = 1 - z, \quad \rho^j = \frac{1-\alpha}{\alpha} + z, \tag{3.5}$$

$$\left.\begin{aligned} T^j = 1, \quad u_z^j = 0 \quad \text{on } z = 0, \\ T^j = 0, \quad u_z^j = 0 \quad \text{on } z = 1. \end{aligned}\right\} \tag{3.6}$$

4. Dispersion equation

4.1. *Derivation of the equation*

We now examine the stability of the basic solution (3.5) by substituting

$$p^j = 1 - \frac{1-\alpha}{\alpha} z - \frac{z^2}{2} + \Pi^j, \quad T^j = 1 - z + \Theta^j, \quad \rho^j = \frac{1-\alpha}{\alpha} + z + R^j,$$

into (3.2), where $\Pi^j, \Theta^j, R^j(\boldsymbol{r}, t) \to 0$ are small perturbations of the p, T and ρ. The fluid velocity is also assumed to be small, $\boldsymbol{u}^j \to 0$. After neglecting second-order small quantities and eliminating q^{fm} between (3.2), we obtain the linearized equations

$$R^j = -\Theta^j, \quad \boldsymbol{u}^j = -\kappa^j(\nabla \Pi^j + R^j \boldsymbol{e}_z), \tag{4.1}$$

$$\left.\begin{aligned} \kappa^j \left(\nabla^2 \Pi^j - \nabla_z \Theta^j\right) = \frac{b^j \kappa^m}{B_1}(\Pi^f - \Pi^m), \\ S^j \partial_t \Theta^j + \kappa^j(\nabla_z \Pi^j - \Theta^j) = \frac{\kappa^j}{Ra^j} \nabla^2 \Theta^j - \frac{b^j \Lambda^m}{\overline{Ra} B_2}(\Theta^f - \Theta^m), \end{aligned}\right\} \tag{4.2}$$

where (4.2) form a closed system of four linear partial differential equations for Π^j and Θ^j, and the fluid densities and velocities can be expressed in terms of Π^j and Θ^j using (4.1).

Separating the variables, we present the solution to (4.2) in the form

$$\Pi^j = \Pi_0^j(z)\zeta, \quad \Theta^j = \Theta_0^j(z)\zeta, \quad \zeta = \exp(\mathrm{i}(k_x x + k_y y) + \Omega t), \tag{4.3}$$

where k_x and k_y are the wavenumbers and Ω is the growth rate. We assume that k_x and k_y are real numbers. This implies that the perturbations are not brought from infinity ($x, y \to \infty$), so the convection is not generated by an external force. Substituting (4.3) into (3.6) and (4.2), we obtain

$$\left.\begin{aligned} \kappa^j \left(\frac{\mathrm{d}^2 \Pi_0^j}{\mathrm{d}z^2} - k_{xy}^2 \Pi_0^j - \frac{\mathrm{d}\Theta_0^j}{\mathrm{d}z}\right) - \frac{b^j \kappa^m}{B_1}(\Pi_0^f - \Pi_0^m) = 0, \\ \Omega S^j \Theta_0^j + \kappa^j \left(\frac{\mathrm{d}\Pi_0^j}{\mathrm{d}z} - \Theta_0^j\right) - \frac{\kappa^j}{Ra^j}\left(\frac{\mathrm{d}^2 \Theta_0^j}{\mathrm{d}z^2} - k_{xy}^2 \Theta_0^j\right) \\ + \frac{b^j \Lambda^m}{\overline{Ra} B_2}(\Theta_0^f - \Theta_0^m) = 0, \end{aligned}\right\} \tag{4.4}$$

with the boundary conditions

$$\Theta_0^j = 0, \quad \frac{\mathrm{d}\Pi_0^j}{\mathrm{d}z} = 0 \quad \text{on } z = 0 \quad \text{and} \quad z = 1, \tag{4.5}$$

where $k_{xy}^2 = k_x^2 + k_y^2$ denotes the overall horizontal wavenumber. Without loss of generality, we assume that $k_{xy} \geq 0$ because this wavenumber enters (4.4) only as k_{xy}^2.

A non-trivial solution to the eigenvalue problem given by (4.4) and (4.5) exists for particular values of the spectral parameter Ω. For boundary conditions considered in this paper (4.5), the non-trivial solution to the conjugate problem can be written in the following simple form (Davis 1969):

$$\Theta_0^j = \delta\Theta^j \sin(k_z z), \quad \Pi_0^j = \delta\Pi^j \cos(k_z z), \quad k_z = \pi n, \quad n = 1, 2, 3, \ldots, \tag{4.6}$$

where k_z is a real number that takes discrete values, and the constant amplitudes $\delta\Pi^j$ and $\delta\Theta^j$ are still unknown. To determine $\delta\Pi^j$ and $\delta\Theta^j$, we substitute (4.6) into (4.4). This yields

$$\left.\begin{aligned} \left(k^2\kappa^j + \frac{\kappa^m}{B_1}\right)\delta\Pi^j + k_z\kappa^j\delta\Theta^j - \frac{\kappa^m}{B_1}\delta\Pi^i = 0, \\ -k_z\kappa^j\delta\Pi^j + \left(\Omega S^j - \kappa^j + k^2\frac{\kappa^j}{Ra^j} + \frac{\Lambda^m}{\overline{Ra}B_2}\right)\delta\Theta^j - \frac{\Lambda^m}{\overline{Ra}B_2}\delta\Theta^i = 0, \end{aligned}\right\} \tag{4.7}$$

where we introduce the notation $k^2 = k_{xy}^2 + k_z^2$ and $i = f, m$, $i \neq j$.

Equations (4.7) form a homogeneous system of linear equations with respect to $\delta\Pi^j$ and $\delta\Theta^j$. There is a non-trivial solution if the matrix of coefficients for (4.7) is singular. By calculating and equating to zero the determinant of the matrix and carrying out identity transformations, we obtain the following dispersion relation:

$$D^f D^m + \left(D^f + D^m\right) Z^c = 0, \tag{4.8}$$

where we denote

$$D^j = \Omega S^j + \kappa^j\left(\frac{k^2}{Ra^j} - \frac{k_{xy}^2}{k^2}\right), \quad Z^c = \frac{\Lambda^m}{\overline{Ra}B_2} - \frac{\kappa^f\kappa^m}{k^2\kappa^f B_1 + 1}\frac{k_z^2}{k^2}. \tag{4.9a,b}$$

The equation $D^j = 0$ is the dispersion relation in the HRL problem for the regular single porosity medium Φ^j, assuming zero mass and heat exchange with the adjacent medium.

Assuming that $D^f + D^m \neq 0$, (4.8) can be written as

$$\frac{D^f D^m}{D^f + D^m} = -Z^c. \tag{4.10}$$

The left-hand side of (4.10) is proportional to the harmonic mean of D^j, reflecting that the mass and heat transfer through DPM occur in parallel through Φ^f and Φ^m. This is analogous to parallel conductors (Nield & Simmons 2007).

Taking into account (4.8) and (4.9), we derive from (4.1) and (4.7) the following relationships for the amplitudes:

$$D^f\delta\Theta^f + D^m\delta\Theta^m = 0, \tag{4.11}$$

$$\delta\Pi^j = \frac{1}{\kappa^j k_z}\left(-\frac{\kappa^j}{D^j}\frac{k_z^2}{k^2} - \frac{1}{Z^c}\left(\frac{\Lambda^m}{\overline{Ra}B_2} - Z^c\right)\right) D^j\delta\Theta^j, \tag{4.12}$$

$$\left.\begin{aligned} \delta u_z^j &= \left(\frac{\kappa^j}{D^j}\frac{k_{xy}^2}{k^2} - \frac{1}{Z^c}\left(\frac{\Lambda^m}{\overline{Ra}B_2} - Z^c\right)\right) D^j \delta\Theta^j, \\ \delta q^{fm} &= \frac{\kappa^m}{B_1}\left(\delta\Pi^f - \delta\Pi^m\right) = \frac{1}{Z^c}\left(\frac{\Lambda^m}{\overline{Ra}B_2} - Z^c\right) D^f \delta\Theta^f, \end{aligned}\right\} \tag{4.13}$$

where δu_z^j and δq^{fm} are the amplitudes of u_z and q^{fm} in the solution given by (4.3) and (4.6)

$$u_z^j = \delta u_z^j \sin(k_z z)\zeta, \quad q^{fm} = \delta q^{fm} \cos(k_z z)\zeta. \tag{4.14}$$

4.2. *Geometric interpretation*

In general, the growth rate Ω is a complex number. According to (4.3), if $\mathrm{Re}\,\Omega > 0$, then the perturbation grows, and if $\mathrm{Re}\,\Omega < 0$, then it fades. From (4.9), it follows that (4.8) is a quadratic equation with respect to Ω

$$a_0\Omega^2 + a_1\Omega + a_2 = 0, \tag{4.15}$$

which coefficients are given by

$$a_0 = S^f S^m, \quad a_1 = S^f Z^m + S^m Z^f + \overline{S}Z^c, \quad a_2 = Z^f Z^m + Z^f Z^c + Z^m Z^c, \tag{4.16a–c}$$

$$Z^j = \kappa^j\left(\frac{k^2}{Ra^j} - \frac{k_{xy}^2}{k^2}\right) = D^j - \Omega S^j, \quad j = f, m. \tag{4.17}$$

We apply the Routh–Hurwitz stability criterion to the characteristic polynomial (4.15) to determine the parameters corresponding to $\mathrm{Re}\,\Omega \le 0$. The inequality $a_0 > 0$ holds because $S^j > 0$. Therefore, the thermal stratification is stable if and only if all leading principal minors of the Hurwitz matrix are positive. This leads to the inequalities $a_1 \ge 0$ and $a_2 \ge 0$, or using the notations of (4.16*b*,*c*), to

$$S^f Z^m + S^m Z^f + \overline{S}Z^c \ge 0, \quad Z^f Z^m + Z^f Z^c + Z^m Z^c \ge 0. \tag{4.18a,b}$$

In the space $\{Z^f, Z^m, Z^c\}$, the equations $a_1 = 0$ and $a_2 = 0$ define a plane and a circular conical surface, respectively (figure 2). The origin is the only point of intersection of these surfaces. Indeed, if we express Z^c from the equation $a_1 = 0$ and substitute it into the equation $a_2 = 0$, then we obtain

$$(Z^f)^2 S^m + (Z^m)^2 S^f = 0.$$

This equation is satisfied only if both $Z^f = 0$ and $Z^m = 0$, and according to (4.16*b*,*c*), $Z^c = 0$. Thus, the plane $a_1 = 0$ splits the conical surface $a_2 = 0$ into the upper and lower parts, which contain the intervals $Z^c > 0$ and $Z^c < 0$ of the axis Z^c, respectively. The inequality $a_1 \ge 0$ constrains the upper region above the plane, and the inequality $a_2 \ge 0$ constrains the region inside the conical surface (figure 2). Therefore, the parameters of stable layers, in which convection does not occur, coincide with the interior of the upper conical surface given by (4.18). If $\overline{Ra} \to 0$, then all solutions to (4.8) satisfy inequalities (4.18) because if the dimensional temperature gradient α_0 approaches 0, then the thermal stratification is stable. This means that the locus of the solution for each $n = \mathrm{const}$ is a curve lying inside the conical surface at $\overline{Ra} \to 0$ (figure 2, curve 1). Each curve can be parameterized by either k_{xy} or Ω. With rising $\overline{Ra}$, i.e. with increasing temperature

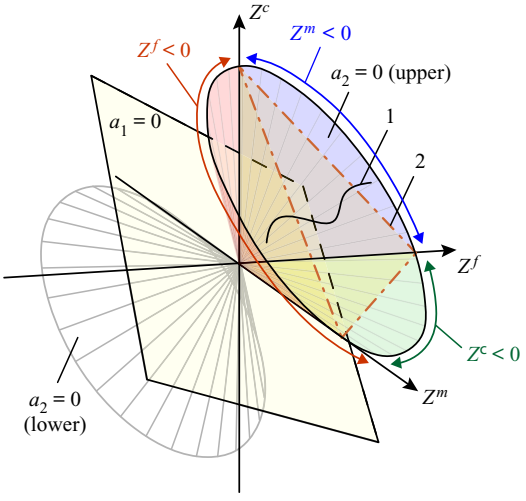

FIGURE 2. Sketch of the locus of solutions to the dispersion equation in the $\{Z^f, Z^m, Z^c\}$ space (curve 1) and key surfaces defining the onset of convection. The coordinate axes belong to the conical surface $a_2 = 0$.

gradient α_0, one of these curves (further analysis of solutions to (4.8) shows that it is with $n = 1$) approaches the boundary of (4.18*b*), and it first intersects the boundary at the critical Rayleigh number, $\overline{Ra}_c$. If $\overline{Ra} > \overline{Ra}_c$, then a segment of such curve corresponding to growing perturbations lies outside the stability region (4.18). At $\overline{Ra} = \overline{Ra}_c$, the locus touches exactly the conical surface $a_2 = 0$ and not the plane surface $a_1 = 0$. Therefore, the inequality (4.18*b*) is more relevant than (4.18*a*) because it is this inequality that is violated at $\overline{Ra} = \overline{Ra}_c$. The critical number $\overline{Ra}_c$ is the minimum $\overline{Ra}$ for which the equation $a_2 = 0$ has a solution.

According to (4.15) and (4.16), the monotonic (not oscillatory) instability of the basic state (3.6) develops at near-critical parameters, $\overline{Ra} \to \overline{Ra}_c+$. This means that if $\mathrm{Re}\,\Omega \to 0$ (or $a_2 \to 0$), then $\mathrm{Im}\,\Omega \equiv 0$. Indeed, if $a_2 \to 0$, then the discriminant of (4.15) is not negative, and therefore, both solutions to (4.15) are real numbers.

5. Sufficient stability conditions

To assist interpretation of the numerical solutions to (4.8) presented in § 7, it is worth considering several asymptotic cases for (4.8) to explicitly show some not obvious features of the convection. For this reason, we present the sufficient stability conditions in § 5 and several particular solutions to (4.8) in § 6.

To satisfy (4.18), it is sufficient to satisfy the three more simple inequalities simultaneously for all k_x, k_y and k_z

$$Z^f \geq 0, \quad Z^m \geq 0, \quad Z^c \geq 0. \tag{5.1}$$

Therefore, these inequalities are sufficient conditions for stability of the stratification (3.6), i.e. for the absence of convection. The conditions (5.1) mean that parameters of all perturbations (4.3) in the $\{Z^f, Z^m, Z^c\}$ space lie inside the conical surface for which the directrix is the triangle with vertices belonging to each of three coordinate axes (figure 2, surface 2). The geometrical interpretation of the sufficient conditions is as follows: if the

locus of solutions to (4.8) lies inside that conical surface, then it also lies inside the circular conical surface $a_2 = 0$.

According to (4.17), the inequality $Z^j \geq 0$ is identical to the following:

$$Ra^j \leq k^4/k_{xy}^2. \tag{5.2}$$

To satisfy (5.2) for all k_x, k_y and k_z, one must determine those wavenumbers that minimize the right-hand side of (5.2) and set Ra^j less than that minimum. For every discrete value of $k_z = \pi n$, the minimum $4\pi^2 n^2$ of the k^4/k_{xy}^2 ratio is reached at $k_{xy} = \pi n$ (Horton & Rogers 1945). Therefore, if

$$Ra^j \leq 4\pi^2 n^2, \tag{5.3}$$

then (5.2) holds for corresponding n. The inequality (5.3) is identical to the stability condition for a homogeneous medium. Consequently, the sign of the quantity Z^f (or Z^m) defines the stability of the basic state (3.5) in the medium Φ^f (or Φ^m), if it is assumed to be isolated from the other medium Φ^m (or Φ^f). If $Z^j \geq 0$ for all k_x, k_y and $k_z = \pi n$, then the conduction state in the isolated medium Φ^j is stable, and if $Z^j < 0$, then convection occurs.

According to (4.9*b*), the inequality $Z^c \geq 0$ is identical to the following:

$$\overline{Ra} \leq \frac{\Lambda^m(k^2\kappa^f B_1 + 1)}{\kappa^f \kappa^m B_2}\frac{k^2}{k_z^2}. \tag{5.4}$$

The right-hand side of (5.4) is the increasing function of k_{xy}^2 (if $k_{xy}^2 \geq 0$); therefore, it reaches a minimum at $k_{xy}^2 = 0$. Consequently, inequality (5.4) for every $k_z = \pi n$ reduces to

$$\overline{Ra} \leq \frac{\Lambda^m(\pi^2 n^2 \kappa^f B_1 + 1)}{\kappa^f \kappa^m B_2}. \tag{5.5}$$

If (5.5) holds, then the inequality $Z^c \geq 0$ is satisfied for all k_x, k_y and $k_z = \pi n$.

The inequalities (5.3) and (5.5) are most restrictive for the first mode, i.e. if $n = 1$. In this case, the conditions (5.3) and (5.5) reduce to

$$Ra^j \leq 4\pi^2, \quad \overline{Ra} \leq \frac{\Lambda^m(\pi^2\kappa^f B_1 + 1)}{\kappa^f \kappa^m B_2}. \tag{5.6a,b}$$

The simultaneous fulfilment of inequalities (5.6) is the sufficient condition for the absence of convection. The inequality (5.6*a*) means that both conduction states in isolated Φ^f and Φ^m are stable; however, this does not guarantee stability for DPM. As shown in §§ 6.4 and 7, the intriguing observation is that, even if the states in Φ^j are stable, the thermal stratification in DPM can be unstable to a perturbation such that $Z^f > 0$, $Z^m > 0$, and $Z^c < 0$ (figure 2). It is sufficient to satisfy the inequality (5.6*b*) to guarantee the stability to all such perturbations.

6. Particular solutions to the dispersion equation

In what follows in §§ 6–8, we assume that (2.6) holds. Then, all parameters in the relations (4.9*b*) and (4.17) for Z^c, Z^f and Z^m can be expressed by using only four

dimensionless quantities – $\overline{Ra}$, κ, Λ and B

$$\left.\begin{aligned} &\kappa^f \equiv \kappa, \quad \kappa^m = 1-\kappa, \quad \Lambda^f \equiv \Lambda, \quad \Lambda^m = 1-\Lambda, \\ &B_1 \equiv B_2 \equiv B, \quad Ra^f = \overline{Ra}\frac{\kappa}{\Lambda}, \quad Ra^m = \overline{Ra}\frac{1-\kappa}{1-\Lambda}. \end{aligned}\right\} \tag{6.1}$$

Consequently, $\overline{Ra}_c$ depends only on κ, Λ and B, according to the most restrictive condition (4.18*b*). Further, we investigate this dependence and associated flow regimes immediately above criticality at $\overline{Ra} \to \overline{Ra}_c+$. We investigate the dependence $\overline{Ra}_c(\kappa, \Lambda, B)$ analytically in this section for particular asymptotic cases and numerically in § 7. We also assume that $n = 1$ because for larger $n \geq 2$, the number $\overline{Ra}_c$ is larger than that for $n = 1$. This assumption is in agreement with the discussion in § 5, and it is also supported by the numerical solutions to (4.8).

6.1. *Asymptotic* $B \to 0$

Let us consider the layer stability in the asymptotic case $B \to 0$ corresponding to local equilibrium between Φ^j. If $B \to 0$, then according to (4.9*b*), $Z^c \to \infty$. Consequently, the dispersion equation (4.8) can be satisfied only if $D^f + D^m \to 0$ because Z^f and Z^m are independent of B. Substituting (3.4) and (4.9*a*) into the equation $D^f + D^m = 0$, we obtain the dispersion relation at $B = 0$

$$\Omega\overline{S} + \frac{k^2}{\overline{Ra}} - \frac{k_{xy}^2}{k^2} = 0. \tag{6.2}$$

This equation is the dispersion relation for EPM (Horton & Rogers 1945). Therefore, the conduction state (3.6) at $B = 0$ is stable at $\overline{Ra} \leq 4\pi^2$ and unstable otherwise at $\overline{Ra} > 4\pi^2$. This yields

$$\overline{Ra}_c \to 4\pi^2, \quad k_c \to \pi \quad \text{as } B \to 0, \tag{6.3}$$

where k_c is the critical overall horizontal wavenumber k_{xy}. The relations (6.3) are the consequence of DPM equivalence to EPM in the case of local equilibrium at $B \to 0$.

6.2. *Asymptotic* $B \to \infty$

We now consider the system behaviour in the asymptotic case $B \to \infty$ corresponding to infinite time required for reaching local equilibrium. Thus, the heat and mass exchange between Φ^j are absent, and the media can be considered isolated from each other. The local equilibrium is never reached in the case of $B \to \infty$. As noted in § 3, a realistic porous medium cannot be characterized with large values of B, but from the mathematical point of view, the asymptotic $B \to \infty$ allows for simple conclusions to be reached that, as we will show, do extrapolate into the region of finite $B \sim 1$.

If $B \to \infty$, then according to (4.9*b*), $Z^c \to 0$ and (4.8) reduces to

$$D^f D^m = 0$$

or according to (4.17), to

$$Z^f Z^m = 0$$

in the case of neutral stability ($\Omega = 0$). Thus, in the asymptotic case $B \to \infty$, the convection develops at the minimum $\overline{Ra}$ for which either $Z^f = 0$ or $Z^m = 0$ is satisfied. If the condition $Z^f = 0$ (or $Z^m = 0$) is reached first with increasing $\overline{Ra}$, then the state (3.6)

in Φ^f (or Φ^m) becomes unstable and convection appears in Φ^f (or Φ^m). At the same time, the stratification in the adjacent medium Φ^m (or Φ^f) remains stable. According to (5.3), $Z^j = 0$ is satisfied if $Ra^j = Ra^j_c = 4\pi^2$ and $k_{xy} = k_z = \pi$. Consequently, the following asymptotic relation holds:

$$\overline{Ra}_c \to \min\left(Ra^f_c \frac{\Lambda^f}{\kappa^f}, Ra^m_c \frac{\Lambda^m}{\kappa^m}\right), \quad k_c \to \pi \quad \text{as } B \to \infty. \tag{6.4}$$

Substituting (6.1) into (6.4) yields

$$\overline{Ra}_c \to 4\pi^2 \min\left(\frac{\Lambda}{\kappa}, \frac{1-\Lambda}{1-\kappa}\right) \le 4\pi^2 \quad \text{as } B \to \infty. \tag{6.5}$$

The minimum of the fractions in (6.5) is not larger than unity for $0 \le \kappa \le 1$ and $0 \le \Lambda \le 1$, and it reaches a maximum at $\kappa = \Lambda$, i.e. if $\overline{K}$ and $\overline{\lambda}$ are distributed in equal proportions between Φ^j. Then, according to (6.5), $\overline{Ra}_c$ reaches the maximum value of $4\pi^2$ in the case of $\kappa = \Lambda$ as compared to other values of κ and Λ. Therefore, we can conclude for $B \to \infty$ that $\overline{Ra}_c$ for DPM does not exceed that for EPM. The onset of convection in DPM occurs for smaller (or equal at $\kappa = \Lambda$) vertical temperature gradients α_0 than that in EPM.

If $\kappa > \Lambda$, then the first fraction within the brackets in (6.5) is smaller than the second one, i.e. convection occurs in Φ^f at $\overline{Ra} \to \overline{Ra}_c+$ ($Ra^f_c = 4\pi^2 > Ra^m_c$). If $\kappa < \Lambda$, then the second fraction in (6.5) is larger, i.e. convection occurs in Φ^m ($Ra^m_c = 4\pi^2 > Ra^f_c$). Thus, we can expect that for any finite and sufficiently large B, where $\overline{Ra} \to \overline{Ra}_c+$, and $\kappa > \Lambda$ (or $\kappa < \Lambda$), the convection pattern in DPM is determined by the flow in the medium Φ^f (or Φ^m) because it is the stratification in this medium that is unstable at $B \to \infty$.

6.3. *Case* $\kappa = \Lambda$

If $\overline{K}$ and $\overline{\lambda}$ are distributed between Φ^f and Φ^m in equal proportions, i.e. $\kappa = \Lambda$, then we derive from (4.9*b*), (4.17), and (6.1)

$$Z^f = \kappa\left(Z^f + Z^m\right), \quad Z^m = (1-\kappa)\left(Z^f + Z^m\right), \quad Z^c = \frac{1-\kappa}{\overline{Ra}B} - \frac{\kappa(1-\kappa)}{\kappa B k^2 + 1}\frac{k_z^2}{k^2}. \tag{6.6}$$

Substituting (6.6) and $\Omega = 0$ into the dispersion equation (4.8) yields

$$\left(Z^f + Z^m\right)\left(\kappa\left(Z^f + Z^m\right) + \frac{1}{\overline{Ra}B} - \frac{\kappa}{\kappa B k^2 + 1}\frac{k_z^2}{k^2}\right) = 0. \tag{6.7}$$

Equation (6.7) is satisfied if either

$$Z^f + Z^m = 0 \quad \text{or} \quad \kappa\left(Z^f + Z^m\right) + \frac{1}{\overline{Ra}B} - \frac{\kappa}{\kappa B k^2 + 1}\frac{k_z^2}{k^2} = 0. \tag{6.8a,b}$$

Which of the two conditions in (6.8) is satisfied first with increasing $\overline{Ra}$ determines $\overline{Ra}_c$ at $\kappa = \Lambda$. Equation (6.8*a*) is the dispersion relation (6.2) for EPM at $\Omega = 0$. It has solutions if $\overline{Ra} \ge 4\pi^2$.

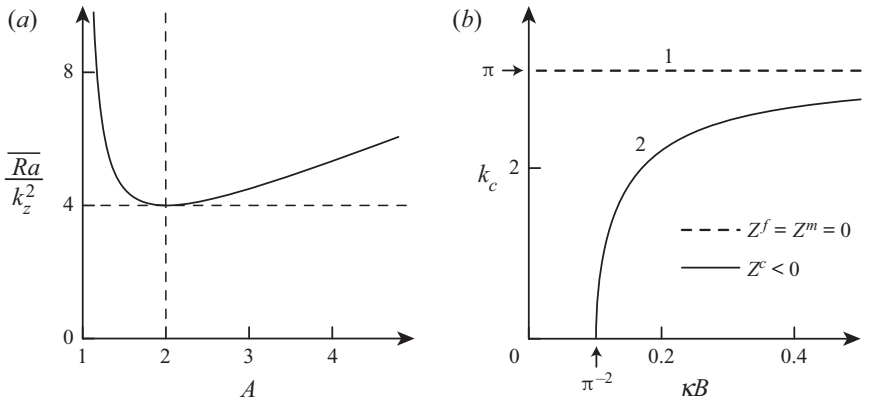

FIGURE 3. (*a*) Value of $\overline{Ra}$ against A as defined by (6.9). (*b*) The critical wavenumbers at $\kappa = \Lambda$.

Substituting (6.6) into (6.8*b*) and collecting the terms, we obtain

$$\frac{\overline{Ra}}{k_z^2} = \frac{A^2}{A-1}, \quad \text{where } A = \frac{\kappa B k^2 + 1}{\kappa B k_z^2} > 1. \tag{6.9}$$

According to (6.9), A is an increasing function of k^2, whereas $\overline{Ra}$ reaches a minimum of $4k_z^2 = 4\pi^2$ at $A = 2$ (figure 3*a*), i.e. at

$$k_{xy}^2 = k_z^2 - \frac{1}{\kappa B} = \pi^2 - \frac{1}{\kappa B}. \tag{6.10}$$

Equation (6.10) has a solution at $\kappa B \geq \pi^{-2}$. Consequently, if $\kappa B \geq \pi^{-2}$, then (6.8) are satisfied simultaneously at $\overline{Ra} = 4\pi^2$, and if $\kappa B < \pi^{-2}$, then (6.8*a*) is satisfied before (6.8*b*) with increasing $\overline{Ra}$. This yields

$$\overline{Ra}_c = 4\pi^2, \quad k_c = \pi \quad \text{or} \quad k_c = \sqrt{\pi^2 - \frac{1}{\kappa B}} \quad \text{at } \kappa = \Lambda. \tag{6.11}$$

Figure 3(*b*) shows the critical wavenumbers (6.11) as solutions to (6.7). Straight line 1 and curve 2 are the solutions with $Z^c > 0$ and $Z^c < 0$ to (6.8*a*) and (6.8*b*), respectively. The critical Rayleigh number is $4\pi^2$ for any such solution. As we have shown, only (6.8*a*) has a solution at $\kappa B < \pi^{-2}$. If $B \to 0$ or $B \to \infty$, then in accordance with (6.3) and (6.4), k_c tends to π in both solutions.

In the case of $k_c = \pi$ and $\overline{Ra} = Ra^f = Ra^m = 4\pi^2$, both $Z^f = 0$ and $Z^m = 0$, i.e. the conduction state in both media becomes unstable. Substituting $Z^f = 0$, $Z^m = 0$ and $\Omega = 0$ into (4.11)–(4.13), we obtain

$$\delta\Theta^f = \delta\Theta^m, \quad \delta\Pi^f = \delta\Pi^m, \quad \delta q^{fm} = 0.$$

Thus, the temperature and pressure amplitudes in the media are identical at $k_c = \pi$, $\kappa = \Lambda$, any B and $\overline{Ra} = \overline{Ra}_c$, meaning that the heat and mass transfer between Φ^j is absent. Consequently, the flow pattern is identical to that in EPM.

6.4. *Case $k_{xy} = 0$ (the plane flow regime)*

The dispersion equation (4.8) admits non-trivial solutions with zero horizontal wavenumbers, which do not exist in the case of homogeneous medium. To determine the Rayleigh numbers for which such solutions are possible, we substitute $k_{xy} = 0$ and $\Omega = 0$ into (4.8), designate $\overline{Ra}$ as $\overline{Ra}_p$, and thereby obtain

$$\overline{Ra}_p = \left(\kappa B k_z^2 + 1\right)\left(\Lambda B k_z^2 + 1\right)\frac{1-\Lambda}{\kappa(1-\kappa)B}. \tag{6.12}$$

If $\overline{Ra} > \overline{Ra}_p$, then the problem admits the growing plane perturbations with $k_{xy} = 0$. In what follows, we refer to such a flow pattern as the convection regime P. For $k_z = \pi$ ($n = 1$), it is schematically shown in figure 4 (in central panel P). The flow pattern consists of only the cross-medium convection cell (figure 1). For instance, the fluid can flow upward through Φ^f ($u_z^f > 0$), then into Φ^m ($q^{fm} > 0$) near the upper boundary of the layer ($z = 1$), then downward through Φ^m ($u_z^m < 0$) and, finally, it flows back into Φ^m ($q^{fm} < 0$) near the lower boundary ($z = 0$), thereby closing the cross-medium circulation. At the same time, according to (4.11), the inequality $\Theta^f \geq \Theta^m$ holds at any position vector $\boldsymbol{r}$. The circulation can occur in the opposite direction, and then, $\Theta^f \leq \Theta^m$.

At near-critical conditions, the plane flow regime appears if and only if $\overline{Ra}_c = \overline{Ra}_p$, where $\overline{Ra}_p$ is given by (6.12) with $k_z = \pi$. In general, with increasing $\overline{Ra}$, the thermal stratification can first become unstable with respect to other perturbations with $k_{xy} > 0$. Consequently, the inequality $\overline{Ra}_c \leq \overline{Ra}_p$ holds, and the opposite inequality $\overline{Ra} > \overline{Ra}_p$ is a sufficient condition for instability.

7. Parametric study

7.1. *Flow regime classification*

The numerical investigation of solutions to the dispersion equation (4.8) for $\Omega = 0$ and all possible κ, Λ and B shows that 9 flow regimes can arise at near-critical conditions. First, we discuss in general the convection patterns of these regimes, leaving for §§ 7.2 and 7.3 the description of parameters κ, Λ and B at which they occur.

The 9 regimes are further referred to as F, F_z, C_{fx}, C_f, C_m, C_{mx}, M_z, M and P (figures 4 and 5). The capital F or M refers to the fractures (Φ^f) or matrix (Φ^m) medium that is unstable at $\overline{Ra} \to \overline{Ra}_c$, respectively. The capital C refers to the counter-rotating pattern that appears at $Z^c < 0$ (see § 5). The capital P corresponds to the plane regime considered in § 6.4. The regimes whose designation includes either the capital F (or M) or the subscript f (or m) are controlled mostly by the convective heat transfer through Φ^f (or Φ^m). The regimes whose designation differs only by the presence of the subscript x (or z) are the same except of the sign for u_x^j (or u_z^j) in one of the media. For further discussion it is convenient to organize the regimes into 4 groups, namely, the co-rotating regimes F and M; the counter-rotating regimes C_f and C_m; the intermediate regimes F_z, C_{fx}, C_{mx} and M_z that appear in transition from co-rotating to counter-rotating patterns; and the regime P (figure 5).

The flow patterns and corresponding distributions of Θ^j and Π^j are schematically shown in figure 4. The diagram in figure 5 shows which flow pattern transitions are possible with continuous changes of the quantities κ, Λ and B. For example, the regime F can change only to M, F_z or P. In other words, the region of parameters in the $\{\kappa, \Lambda, B\}$ space corresponding to the regime F can have boundaries only with the regions corresponding to M, F_z and P.

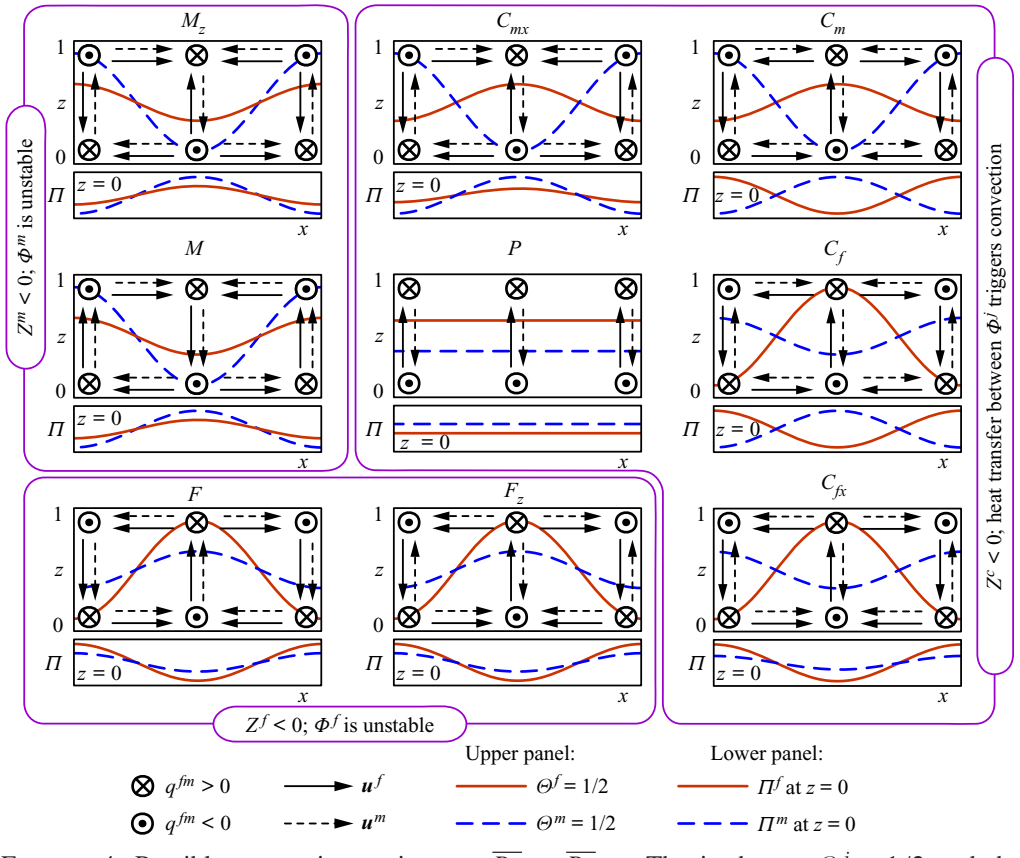

FIGURE 4. Possible convection regimes at $\overline{Ra} \to \overline{Ra}_c+$. The isotherms $\Theta^j = 1/2$ and the direction of flow in convection cells are schematically shown in the upper panel for every regime. The pressure distributions, $\Pi^j(x)$, at the lower boundary $z = 0$ are shown in the lower panels.

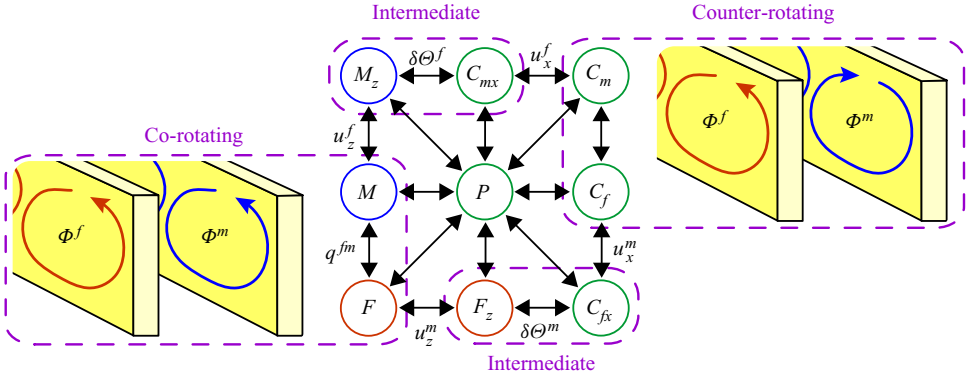

FIGURE 5. Possible transitions of the flow regimes. The dashed lines group the regimes in pairs of identical convection patterns in Φ^j but with different amplitudes $\delta\Pi^j$ and $\delta\Theta^j$ for $j = f, m$. The labels u_x^j, u_z^j, q^{fm} and $\delta\Theta^j$ designate transitions in which only the corresponding parameter changes sign.

The regimes F and F_z correspond to the inequality $Z^f < 0$ at $\overline{Ra} = \overline{Ra}_c$, i.e. if the locus of solutions to (4.8) touches the conical surface $a_2 = 0$ at $Z^f < 0$ (figure 2). Numerical analysis of the solutions to (4.8) indicates that these regimes can arise only if $\kappa \geq \Lambda$, i.e. if Φ^f determines the flow pattern ($Ra^f \geq 4\pi^2 \geq Ra^m$). This is in agreement with the theoretical analysis of the asymptotic case $B \to \infty$ discussed in § 6.2. In the regimes F and F_z, the convection in DPM is triggered by the unstable conduction state in Φ^f and the flow in Φ^m appears only due to heat and mass transfer between the media. Therefore, and according to (4.11), in which $D^j = Z^j$ at $\Omega = 0$, the absolute value of the temperature amplitude in Φ^f is larger than that in Φ^m ($|\delta\Theta^f| > |\delta\Theta^m|$).

Similarly, the regimes M and M_z correspond to the inequality $Z^m < 0$ at $\overline{Ra} = \overline{Ra}_c$, i.e. if the locus touches the conical surface $a_2 = 0$ at $Z^m < 0$. As in the asymptotic case $B \to \infty$, these regimes can arise only if $\kappa \leq \Lambda$, i.e. if Φ^m determines the flow pattern ($Ra^m \geq 4\pi^2 \geq Ra^f$). The convection in these regimes is triggered by the unstable state in Φ^m, and the flow in Φ^f appears only due to heat and mass transfer between the media. Therefore, and according to (4.11), the absolute value of the temperature amplitude in Φ^m is larger than that in Φ^f ($|\delta\Theta^m| > |\delta\Theta^f|$).

According to (4.11), in which $D^j = Z^j$ at $\Omega = 0$, the temperature amplitudes $\delta\Theta^f$ and $\delta\Theta^m$ have identical signs for F, F_z, M and M_z. Thus, higher (or lower) temperatures in Φ^f correspond to higher (or lower) temperatures in Φ^m in all 4 regimes.

The other 5 regimes – C_{fx}, C_f, C_m, C_{mx} and P – correspond to the inequality $Z^c < 0$ at $\overline{Ra} = \overline{Ra}_c$, i.e. if the locus of solutions to (4.8) touches the surface $a_2 = 0$ at $Z^c < 0$. These regimes can arise at both $\kappa > \Lambda$ and $\kappa < \Lambda$. Therefore, the convection is not determined by only Φ^f or Φ^m, which can result in more complicated flow patterns. For example, according to (4.11), the temperature amplitudes in Φ^f and Φ^m have opposite signs in these regimes ($\delta\Theta^f\delta\Theta^m < 0$), i.e. higher (or lower) temperatures in Φ^f correspond to lower (or higher) temperatures in Φ^m (figure 4). Furthermore, a noteworthy observation is that the conduction states in Φ^f and Φ^m considered apart (isolated from each other) are stable because $Z^f > 0$ and $Z^m > 0$. The convection appears only if Φ^f and Φ^m are merged to form DPM. We can interpret this as that the heat transfer between the media triggers the onset of convection in regimes C_{fx}, C_f, C_m, C_{mx} and P.

The co-rotating regimes F and M are characterized with qualitatively similar flow fields, which are a simple generalization of the cellular convection cells in homogeneous porous medium, i.e. EPM (Nield & Bejan 2017). Horizontal and vertical components of the fluid velocities in Φ^f and Φ^m for any position vector $\boldsymbol{r}$ have equal signs corresponding to co-rotating cells in both media (figure 4). The regimes F and M differ only in the direction of fluid flow between Φ^j and the amplitudes $\delta\Pi^j$ and $\delta\Theta^j$. In the regime F (or M), the convection in Φ^f (or Φ^m) dominates over that in Φ^m (or Φ^f), leading to larger absolute values of $\delta\Theta^f$ and $\delta\Pi^f$ (or $\delta\Theta^m$ and $\delta\Pi^m$). At the same time, in the regime F, the medium Φ^f withdraws fluid from Φ^m at the bottom of ascending currents due to lower pressure Π^f ($q^{fm} < 0$ at $z = 0$) and returns it back to Φ^m at the top of the currents ($q^{fm} > 0$ at $z = 1$).

Let us consider how the flow pattern changes with varying κ, Λ and B in the following sequence of transitions (corresponding to the counter-clockwise movement around P in figures 4 and 5):

$$F \to F_z \to C_{fx} \to C_f. \tag{7.1}$$

The transition from the co-rotating regime F to the intermediate regime F_z is characterized by increasing intensity of the fluid withdrawal at the bottom of the ascending current. When entering the regime F_z, the withdrawal becomes so intense that it reverts the vertical direction of flow in Φ^m. Now, the fluid in Φ^m converges to the bottom of ascending currents

in Φ^f, which can be considered as sink zones for the medium Φ^m. Similarly, the top of ascending currents in Φ^f are the source zones for Φ^m from which the flow diverges through Φ^m. Thus, the transition from F to F_z breaks down convection cells in Φ^m and leads to the appearance of new cross-media cells as in the P regime. At every $x, y = \text{const}$ in the cross-media cells, the fluid ascends through Φ^f (or Φ^m) and flows to the adjacent medium Φ^m (or Φ^f) at the top of ascending currents, then it flows down in the descending currents through the medium Φ^m (or Φ^f), and ultimately flows back to Φ^f (or Φ^m) at $z = 0$, closing the circulation (figure 1).

The intermediate regimes F_z and C_{fx} have identical convection patterns and different temperature distributions in Φ^m. Transition from F_z to C_{fx} is characterized by increasing influence of convective heat transfer through Φ^m as compared to that between Φ^j. Consequently, the temperature amplitude $\delta\Theta^m$ changes its sign when entering C_{fx}, and the inequality $\delta\Theta^f\delta\Theta^m < 0$ holds in the regime C_{fx}. Now, the descending (or ascending) currents in Φ^m move the isotherms $\Theta^m = \text{const}$ downward (or upward).

The transition from C_{fx} to C_f is characterized by a further increasing influence of the reversed flow direction in Φ^m. At the transition, the horizontal velocity in Φ^m changes its sign, and new cellular convection with opposite direction of circulation forms in Φ^m. Thus, the flow pattern in the regime C_f consists of counter-rotating cells in the media Φ^f and Φ^m. At the same time, the cross-medium convection cells also exist (figure 4).

The flow fields in regimes C_f and C_m are qualitatively similar, with different amplitudes of pressure and temperature. The temperature amplitudes $\delta\Theta^f$ and $\delta\Theta^m$ have opposite signs ($\delta\Theta^f\delta\Theta^m < 0$) reflecting the counter-rotating behaviour of convection. Here, the dominant feature is the convective heat transfer through the media that moves the isotherms in Φ^f and Φ^m in opposite directions. The heat transfer between Φ^j does not significantly affect $\delta\Theta^j$ because it is secondary. By definition, the boundary between C_f and C_m corresponds to equal absolute values of $\delta\Theta^f$ and $\delta\Theta^m$. The inequalities $|\delta\Theta^f| > |\delta\Theta^m|$ and $|\delta\Theta^f| < |\delta\Theta^m|$ hold in regimes C_f and C_m, respectively. Transition from C_f to C_m is characterized by increasing influence of convective heat transfer through Φ^m as compared to that through Φ^f. From now on, if we consider the regimes C_m, C_{mx}, M_z and M (figure 4), the convection in Φ^m determines the flow pattern.

The transition sequence

$$M \to M_z \to C_{mx} \to C_m$$

is characterized by the processes in the media Φ^m and Φ^f, which mirror the processes in the media Φ^f and Φ^m in the sequence (7.1) described in detail above. In short, when entering M_z from M, the vertical velocity u_z^f in Φ^f changes sign. When entering C_{mx}, the temperature amplitude $\delta\Theta^f$ changes sign. When entering C_m, the horizontal velocity u_x^f in Φ^f reverts direction and cellular convection in Φ^f with an opposite direction of circulation forms (figure 5).

7.2. *Solution map at $B = \text{const}$*

Now, we constrain the regions of the $\{\kappa, \Lambda, B\}$ space corresponding to each convection regime. First, we consider the numerical solutions to the dispersion equation (4.8) for fixed B and different κ and Λ (figure 6). The numerical solution indicates that only the transitions shown in figure 5 are possible. The straight line $\kappa = \Lambda$ for any B is the boundary between a pair of flow regimes. In agreement with the asymptotic case $B \to \infty$ (see § 6.2), regimes F and F_z can arise only at $\kappa \geq \Lambda$, i.e. below the straight line $\kappa = \Lambda$, whereas M and M_z can arise only at $\kappa \leq \Lambda$, i.e. above the straight line $\kappa = \Lambda$. The regimes C_{fx}, C_f, C_m, C_{mx} and P can arise near the straight line $\kappa = \Lambda$ and in a wider region at $\Lambda > \kappa > 1/2$.

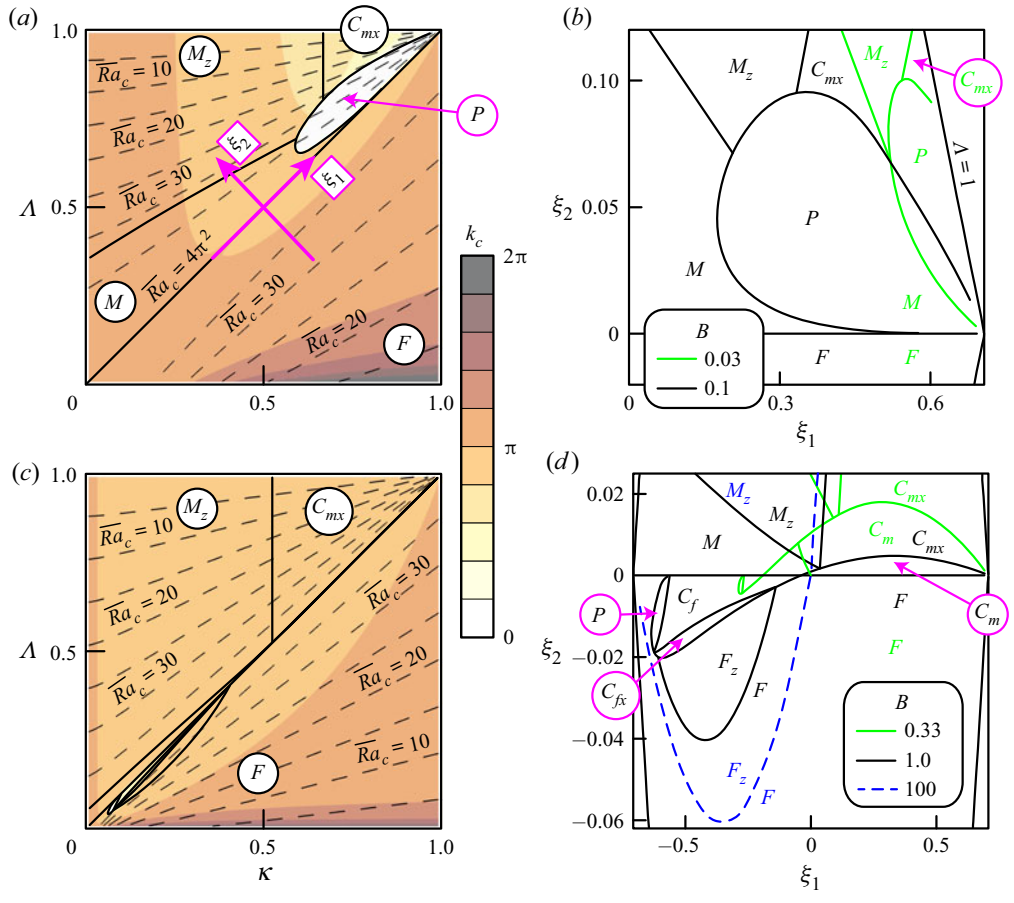

FIGURE 6. Solutions to the dispersion equation for (*a*,*b*) $B = 0.1$ and (*c*,*d*) $B = 1$. The solution maps for other values of B are also shown in the panels (*b*,*d*). The solid lines separate different flow regimes. The dashed lines in (*a*,*c*) are the contour lines of $\overline{Ra}_c$ with step 5.

To make the boundaries of the flow regimes near the straight line $\kappa = \Lambda$ more distinct, we show the solution map in both the $\{\kappa, \Lambda\}$ plane (figure 6*a*,*c*) and the $\{\xi_1, \xi_2\}$ plane (figure 6*b*,*d*), where

$$\xi_1 = \frac{1}{\sqrt{2}}(\kappa + \Lambda - 1), \quad \xi_2 = \frac{1}{\sqrt{2}}(\Lambda - \kappa).$$

Thus, the origin of the $\{\xi_1, \xi_2\}$ plane is the point $\kappa = \Lambda = 1/2$ in the $\{\kappa, \Lambda\}$ plane (figure 6*a*).

As discussed in § 6.1, if $B \to 0$ (i.e. if Φ^j are under local equilibrium), then the solution map contains only two regions $\kappa > \Lambda$ and $\kappa < \Lambda$ corresponding to the regimes F and M, respectively. When B increases from 0 (i.e. the degree of local non-equilibrium increases), the regions M_z, P and C_{mx} appear at $\kappa \to 1$, $\Lambda \to 1$ and $\kappa < \Lambda$ (figure 6*b*, $B = 0.03$). When B increases to 0.1, the regions M_z, C_{mx} and P expand downward and leftward along the straight line $\kappa = \Lambda$ ($\xi_2 = 0$), and the area of the region P reaches a maximum at $B \approx 0.1$ (figure 6*b*).

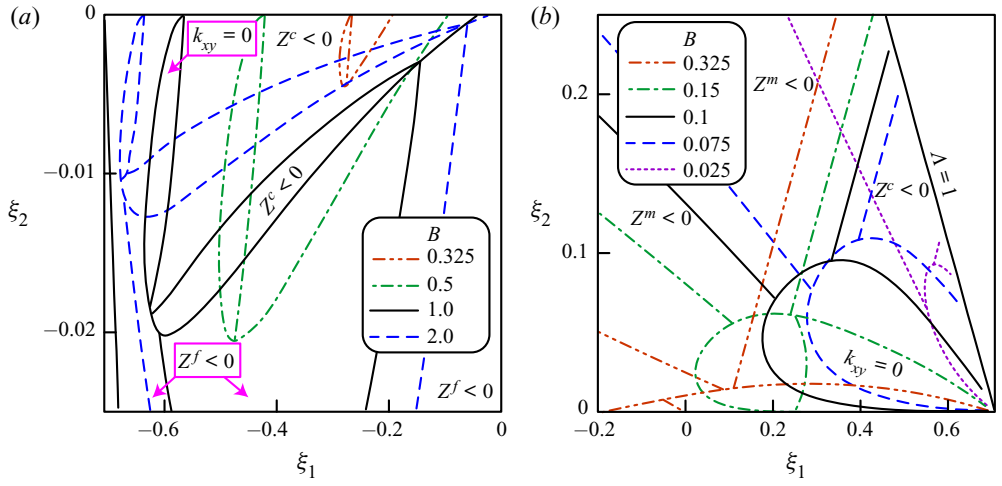

FIGURE 7. Boundaries of the convection regimes in the $\{\xi_1, \xi_2\}$ plane. See figure 6 for reference between the solution map and the convection regimes. The conditions $Z^f < 0$, $Z^m < 0$, $Z^c < 0$ and $k_{xy} = 0$ are satisfied in the corresponding regions bounded by the solid lines.

When B increases from 0.1 to 1, the region $Z^c < 0$, corresponding to the counter-rotating and plane regimes, expands across the straight line $\kappa = \Lambda$ into the region $\kappa > \Lambda$ and $\kappa < 1/2$ (figure 6*c*,*d*). In addition, the region C_m appears inside the envelope curve bounding the region P. Then, the boundary between P and C_m moves downward and leftward (along the straight line $\kappa = \Lambda$ corresponding to equal distributions of $\overline{K}$ and $\overline{\lambda}$ between Φ^j), which results in the disappearance of the region P at $\kappa < \Lambda$. At $\kappa > \Lambda$, the regions F_z, C_{fx} and C_f appear, with the region F_z growing downward from C_{fx}. A more detailed evolution of the solution map near the straight line $\kappa = \Lambda$ when B increases from 0.025 to 2.0 is shown in figure 7.

When B increases from 1 to 100, all regions except F, M_z and C_{mx} shrink to the straight line $\kappa = \Lambda$. The solution map for $B > 100$ is indistinguishable from the map at $B = 100$ shown in figure 6(*d*). According to (4.11) and (4.12), the amplitudes $\delta\Theta^f$ and $\delta\Pi^f$ tend to zero in the region $\kappa < \Lambda$ at $\Omega = 0$ and $B \to \infty$ ($Z^m = 0$ or $Z^c = 0$), and the amplitudes $\delta\Theta^m$ and $\delta\Pi^m$ tend to zero in the region $\kappa > \Lambda$ ($Z^f = 0$ or $Z^c = 0$). Thus, the convection only in Φ^m (or Φ^f) develops if $\kappa < \Lambda$ (or $\kappa > \Lambda$) and $B \to \infty$. This observation agrees with the analytical investigation of the case $B \to \infty$ carried out in § 6.2.

As shown in figure 6(*a*), there is a sharp transition to the regime P from any other regime. When entering the regime P, the wavenumber k_c sharply decreases to 0 and the solution bifurcates to P. At the same time, $\overline{Ra}_c$ changes continuously. Other transitions, which are not into P or across the straight line $\kappa = \Lambda$ (see (6.11)), are continuous rather than sharp bifurcations.

In general, all except two boundaries between the convection regimes at $B = \text{const}$ are curved lines, which cannot be described with a finite readable relationship. The first exception is the straight line $\kappa = \Lambda$. Let us prove that the boundary between M_z and C_{mx}, characterized with the condition $\delta\Theta^f = 0$ (figure 5), is the straight line $\kappa = \text{const}$, i.e. the second exception. The parameters of any point belonging to this line satisfy the following system of equations:

$$Z^m = 0, \quad Z^c = 0, \tag{7.2a}$$

$$\frac{\mathrm{d}}{\mathrm{d}k^2}\left(Z^f Z^m + Z^f Z^c + Z^m Z^c\right) = 0. \tag{7.2b}$$

Equations (7.2*a*) indicate that the line is the boundary between the regimes M_z ($Z^m < 0$ and $Z^c > 0$) and C_{mx} ($Z^m > 0$ and $Z^c < 0$). The dispersion equation (4.8) is satisfied by (7.2*a*). Equation (7.2*b*) indicates that the locus of solutions to (4.8) touches the surface $a_2 = 0$ (figure 2). Here, k^2 is considered as the locus parameter. With account for (7.2*a*), (7.2*b*) simplifies to

$$\frac{\mathrm{d}}{\mathrm{d}k^2}\left(Z^m + Z^c\right) = 0. \tag{7.3}$$

Differentiating (4.9*b*) and (4.17), we obtain

$$\frac{\mathrm{d}Z^m}{\mathrm{d}k^2} = \frac{1-\Lambda}{\overline{Ra}} - (1-\kappa)\frac{k_z^2}{k^2}, \quad \frac{\mathrm{d}Z^c}{\mathrm{d}k^2} = (1-\kappa)\kappa\frac{2k^2\kappa B + 1}{(k^2\kappa B + 1)^2}\frac{k_z^2}{k^4}. \tag{7.4}$$

Substituting (4.9*b*), (4.17) and (7.4) into (7.2*a*) and (7.3), we derive the system of three algebraic equations. After excluding $\overline{Ra}$ and k_{xy}^2 from that system and carrying out identity transformations, we obtain

$$\kappa = \frac{Bk_z^2 + 1}{2Bk_z^2 + 1}. \tag{7.5}$$

For $B = \text{const}$, (7.5) gives a vertical straight line in the plane $\{\kappa, \Lambda\}$ between the regimes M_z and C_{mx}. According to (7.5), if $B = 0$, then $\kappa = 1$, and with increasing B, the boundary between M_z and C_{mx} moves leftward in the plane $\{\kappa, \Lambda\}$ approaching the straight line $\kappa = 1/2$ in the limit $B \to \infty$.

7.3. *Solutions at $\kappa = const$ or $\Lambda = const$*

The solutions to (4.8) for fixed $\kappa = 0.7$ and $\Lambda = 0.7$ are shown in figures 8 and 9, respectively. The style of the contour lines shows the type of solution, either $Z^f < 0$ (regimes F and F_z) or $Z^m < 0$ (regimes M and M_z), or $Z^c < 0$ (regimes C_{fx}, C_f, C_m and C_{mx}), or $k_{xy} = 0$ (regime P). If $B \to 0$, then, in agreement with (6.5), $\overline{Ra}_c \to 4\pi^2$ and $k_c \to \pi$. For any B, the critical Rayleigh number is not higher than $4\pi^2$, and thus, $\overline{Ra}_c$ for DPM does not exceed $\overline{Ra}_c$ for EPM (figures 8*a* and 9*a*). This result demonstrates that DPM differs from BDPM, in which LTNE can increase the value of $\overline{Ra}_c$ (Nield & Kuznetsov 2006). The critical wavenumber k_c can be either higher or lower than π. When entering the regime P, k_c abruptly decreases to 0 and the solution bifurcates into the plane flow pattern (figures 8*b* and 9*b*).

The labels $\Lambda = 0.7+$ and $\kappa = 0.7-$ mean that Λ and κ are slightly less than or higher than 0.7, respectively. The contour lines $\Lambda = 0.7+$ at $\kappa B \geq \pi^{-2}$ and $\kappa = 0.7-$ at $\Lambda B \geq \pi^{-2}$ correspond to the second solution for k_c in (6.11). As shown in figure 3(*b*), the contour lines $\Lambda = 0.7-$ and $\kappa = 0.7+$ would be straight lines $k_c = \pi$ corresponding to the first solution for k_c in (6.11).

The numerical solutions to (4.8) indicate that the conclusions of this section are valid for any constant value of κ or Λ other than 0.7.

8. Numerical experiments

To support the analytical findings of the previous sections, we conduct numerical modelling of convection in DPM using the reservoir simulator MUFITS (Afanasyev

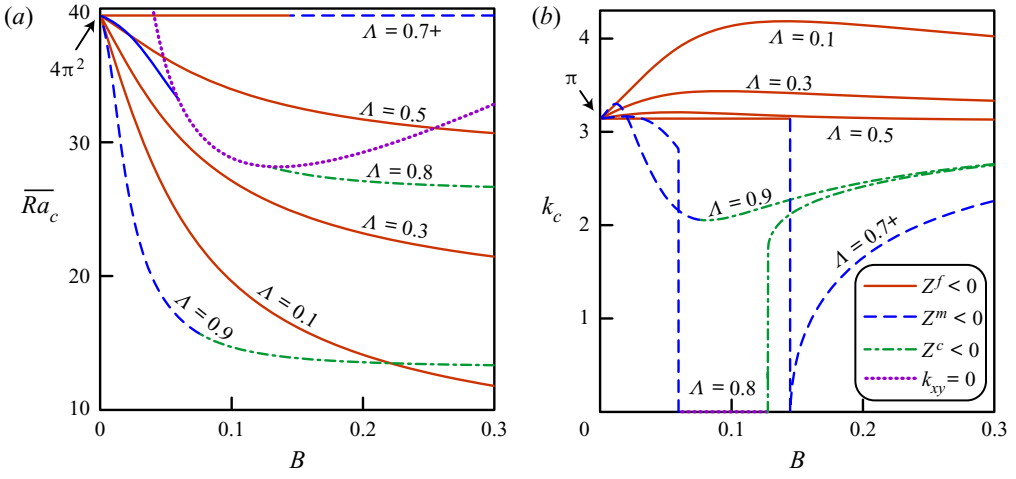

FIGURE 8. Solutions to the dispersion equation at $\kappa = 0.7$ against variable B. The dotted curve is given by (6.12) at $\Lambda = 0.8$.

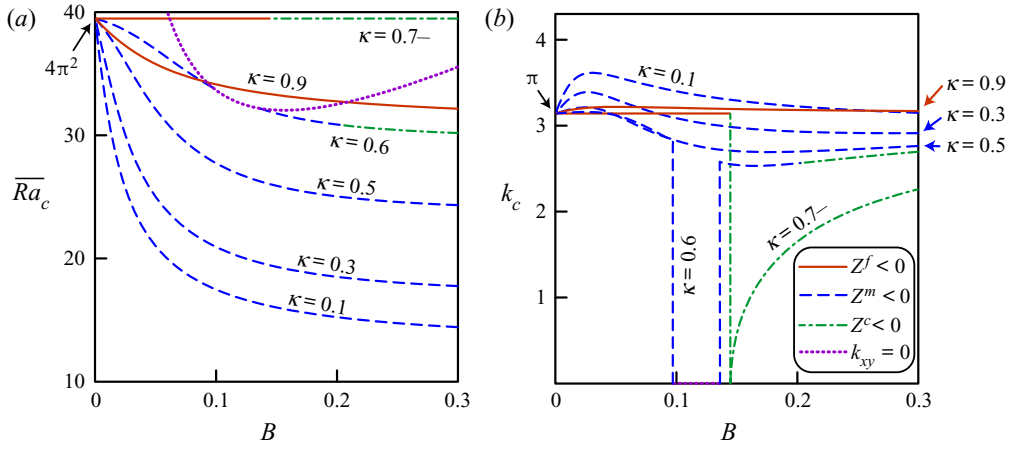

FIGURE 9. Solutions to the dispersion equation at $\Lambda = 0.7$ against variable B. The dotted curve is given by (6.12) at $\kappa = 0.6$.

2017). The simulations are performed using the dual-porosity dual-permeability concept with (2.6) assumed to hold. The system of governing equations used in the modelling, which in the Oberbeck–Boussinesq approximation reduces to (2.1)–(2.4), can be derived from Pruess (1983), Pruess & Narasimhan (1985), Dietrich *et al.* (2005) and Berre, Doster & Keilegavlen (2019). The inequality $\alpha \ll 1$ holds; thus, the Oberbeck–Boussinesq approximation is applicable with a sufficient degree of accuracy.

In dimensionless units, we consider the two-dimensional domain of finite width 5, $x \in [0, 5]$, for which the boundaries $x = 0$ and $x = 5$ are assumed to be impermeable and adiabatic (figure 10). The parameters of 4 considered simulation scenarios are summarized in table 1, whereas other dimensionless quantities are $S^f = 1.5$, $S^m = 3.0$, $\alpha = 3.6 \cdot 10^{-3}$ and $\Upsilon = 2.1 \cdot 10^{-5}$. The $\overline{Ra}$ number is chosen to be less than 10 % higher than $\overline{Ra}_c$ ($\overline{Ra} \leq 1.1\overline{Ra}_c$). Consequently, the layer is at slightly super-critical conditions, for which

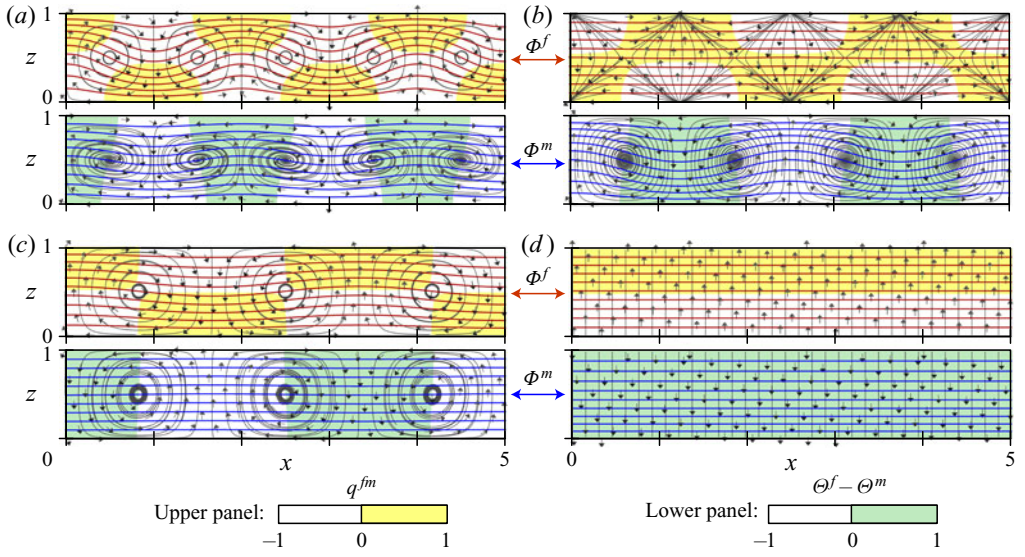

FIGURE 10. (*a–d*) Simulated convection patterns for the regimes F, M_z, C_f and P, respectively. The bold curves show isotherms $\Theta^j = i/10$, $i = 1 \ldots 9$, the thin curves are the streamlines and the arrows indicate the direction of the fluid flow in Φ^f (upper panels) and Φ^m (lower panels), respectively.

Regime	$\overline{Ra}$	κ	Λ	B	$\overline{Ra}_c$	k_c	Figure 10
F	36.904	0.89	0.67	0.1	33.549	3.2175	(*a*)
M_z	22.530	0.50	0.78	0.1	20.481	2.7258	(*b*)
C_f	40.494	0.15	0.14	1.0	38.112	1.9076	(*c*)
P	36.753	0.68	0.75	0.1	33.411	0.0	(*d*)

TABLE 1. Parameters of the considered simulation scenarios.

the theoretical study is presented. Details of the numerical algorithm and the simulation results as well as animated figures showing the convection development are included in the supplementary material available at https://doi.org/10.1017/jfm.2020.462.

The flow patterns evolving at $t > 100$ from the quiescent stratified fluid at $t = 0$ are shown in figure 10. The simulations are in agreement with the analytical study that predicts the appearance of the F, M_z, C_f and P regimes, respectively. Indeed, the simulated patterns replicate those schematically shown in figure 4. Also, the horizontal dimensions of the convection cells are in line with the critical wavelength k_c. According to (4.6) and (4.14), the regions where the heat is transferred from Φ^f to Φ^m by means of convection ($q^{fm} > 0$) and thermal conduction ($\Theta^f - \Theta^m > 0$) do not coincide. An interesting feature is that the streamlines in the convection cells can be spiral curves converging to the cell centres rather than closed curves. This is explained by the mass transfer between Φ^j in the weakly nonlinear regimes at $\overline{Ra}_c < \overline{Ra} \leq 1.1\overline{Ra}_c$.

9. Conclusions

The study shows that Darcy–Bénard convection in a horizontal layer of DPM with isothermal impermeable boundaries can occur by the onset of nine different flow regimes. Most of these regimes are driven by the convective heat transport in both media Φ^j. The regimes include the flow patterns with the co-rotating or counter-rotating convection cells in the adjacent media, as well as the plane flow field with only the cross-medium circulation. We show that the critical Rayleigh number depends on three parameters, namely, the ratios of permeability and heat conductivity in the media and the dimensionless number characterizing the intensity of heat and mass transfer between Φ^j. We provide complete classification of the flow regimes and plot them in the solution map.

In the asymptotic cases of local thermal equilibrium ($B \to 0$) or the absence of heat and mass exchange between Φ^j ($B \to \infty$), only the co-rotating flow regimes, which are a simple generalization of the cellular flow pattern in the HRL problem for homogeneous medium, can arise. The most unexpected counter-rotating and plane convection patterns arise when the heat transfer between Φ^j is comparable to that through the media (i.e. at $0.01 \leq B \leq 10$). However, these regimes occur only if the ratios of permeability and heat conductivity in the media are close to each other ($\kappa \approx \Lambda$). For the considered boundary conditions at $z = 0$ and $z = 1$, the co-rotating convection occurs within a much wider range of parameters.

A noteworthy conclusion for geophysical applications is that the critical Rayleigh number for the fractured-porous medium is not higher than that for the equivalent homogeneous medium. Therefore, the onset of convection in fractured reservoirs occurs for vertical gradients of temperature, which are not higher than that in the homogeneous reservoirs for any parameters of the layer. For a fixed bulk permeability, the fractures reduce the critical Rayleigh number, i.e. the thermal stratification is less stable in a fractured-porous medium than that in the equivalent homogeneous medium. This result agrees with the study by Nield & Simmons (2007), who concluded that heterogeneity of a porous medium leads to reduction of the critical Rayleigh number. We extend it by concluding that the thermal stratification in a fractured-porous medium is most stable if the bulk permeability and the bulk heat conductivity are distributed in equal proportions between fractures and matrix.

The present study can be applied for predicting convection patterns for a variety of geophysical applications, in addition to the numerical studies by Simmons *et al.* (2008), Vujević *et al.* (2014) and others, who also report counter-rotating convection cells, although in a slightly different context. The work still to be done is the study extension to the cases of other boundary conditions at $z = 0$ and $z = 1$. In the geophysical context, the case of open boundary $z = 1$ would be most significant because it corresponds to a hydrothermal system interacting through $z = 1$ with shallow meteoric water. Even the considered case of impermeable isothermal boundaries can further be extended by accounting for anisotropic permeability in Φ^j and $B_1 \neq B_2$. Preliminary study of the $B_1 \neq B_2$ situation shows that the region of counter-rotating and plane regimes at $B_2 =$ const expands significantly with decreasing ratio B_1/B_2. Therefore, the likelihood of such regimes increases if the rate of approaching the local equilibrium for temperatures is lower than that for pressures, but this is a subject of further research.

Acknowledgments

Funding for this work was provided by the RF President's Council on Grants (MD-3567.2018.1).

Declaration of interests

The author reports no conflict of interest.

Supplementary material and movies

Supplementary material and movies are available at https://doi.org/10.1017/jfm.2020.462.

REFERENCES

AFANAS'EV, A. A. 2012 A representation of the equations of multicomponent multiphase seepage. *J. Appl. Math. Mech.* **76** (2), 192–198.

AFANASYEV, A. 2017 Reservoir simulation with the MUFITS code: extension for horizontal wells and fractured reservoirs. *Energy Procedia* **125**, 596–603.

AFANASYEV, A., BLUNDY, J., MELNIK, O. & SPARKS, S. 2018 Formation of magmatic brine lenses via focussed fluid-flow beneath volcanoes. *Earth Planet. Sci. Lett.* **486**, 119–128.

BANU, N. & REES, D. A. S. 2002 Onset of Darcy–Bénard convection using a thermal non-equilibrium model. *Intl J. Heat Mass Transfer* **45** (11), 2221–2228.

BARENBLATT, G. I., ZHELTOV, I. P. & KOCHINA, I. N. 1960 Basic concepts in the theory of seepage of homogeneous liquids in fissured rocks [strata]. *J. Appl. Math. Mech.* **24** (5), 1286–1303.

BERRE, I., DOSTER, F. & KEILEGAVLEN, E. 2019 Flow in fractured porous media: a review of conceptual models and discretization approaches. *Transp. Porous Med.* **130** (1), 215–236.

BROWNELL, D. H., GARG, S. K. & PRITCHETT, J. W. 1977 Governing equations for geothermal reservoirs. *Water Resour. Res.* **13** (6), 929–934.

CHEN, Z. Q., CHENG, P. & ZHAO, T. S. 2000 An experimental study of two phase flow and boiling heat transfer in bi-dispersed porous channels. *Intl Commun. Heat Mass Transfer* **27** (3), 293–302.

DAVIS, S. H. 1969 On the principle of exchange of stabilities. *Proc. R. Soc. Lond.* A **310** (1502), 341–358.

DIERSCH, H. J. G. & KOLDITZ, O. 2002 Variable-density flow and transport in porous media: approaches and challenges. *Adv. Water Resour.* **25** (8–12), 899–944.

DIETRICH, P., HELMIG, R., SAUTER, M., TEUTSCH, G., HÖTZL, H. & KÖNGETER, J. 2005 *Flow and Transport in Fractured Porous Media*. Springer.

ENE, H. I. & SANCHEZ-PALENCIA, E. 1982 On thermal equation for flow in porous media. *Intl J. Engng Sci.* **20** (5), 623–630.

EPHERRE, J. F. 1975 Apparition criteria of natural-convection in a porous anisotropic layer. *Rev. Gén. Therm.* **14** (168), 949–950.

GARG, S. K. & PRITCHETT, J. W. 1977 On pressure-work, viscous dissipation and the energy balance relation for geothermal reservoirs. *Adv. Water Resour.* **1** (1), 41–47.

GÉRARD, A., GENTER, A., KOHL, T., LUTZ, P., ROSE, P. & RUMMEL, F. 2006 The deep EGS (Enhanced Geothermal System) project at Soultz-sous-Forêts (Alsace, France). *Geothermics* **35** (5), 473–483.

GHANBARIAN, B. & DAIGLE, H. 2016 Thermal conductivity in porous media: percolation-based effective-medium approximation. *Water Resour. Res.* **52** (1), 295–314.

HORTON, C. W. & ROGERS, F. T. 1945 Convection currents in a porous medium. *J. Appl. Phys.* **16** (6), 367–370.

KAZEMI, H., MERRILL, L. S., PORTERFIELD, K. L. & ZEMAN, P. R. 1976 Numerical simulation of water-oil flow in naturally fractured reservoirs. *Soc. Petrol. Engng J.* **16** (06), 317–326.

KVERNVOLD, O. & TYVAND, P. A. 1980 Dispersion effects on thermal-convection in porous-media. *J. Fluid Mech.* **99**, 673–686.

LAPWOOD, E. R. 1948 Convection of a fluid in a porous medium. *Proc. Camb. Phil. Soc.* **44** (4), 508–521.

LIM, K. T. & AZIZ, K. 1995 Matrix-fracture transfer shape factors for dual-porosity simulators. *J. Petrol. Sci. Engng* **13**, 169–178.

MAGYARI, E., REES, D. A. S. & KELLER, B. 2005 Effect of viscous dissipation on the flow in fluid saturated porous media. In *Handbook Porous Media*, 2nd edn (ed. K. Vafai), pp. 373–406. Taylor and Francis.

MCKIBBIN, R. & O'SULLIVAN, M. J. 1980 Onset of convection in a layered porous medium heated from below. *J. Fluid Mech.* **96** (2), 375–393.

MCKIBBIN, R. & TYVAND, P. A. 1984 Thermal convection in a porous medium with horizontal cracks. *Intl J. Heat Mass Transfer* **27** (7), 1007–1023.

NIE, R. S., MENG, Y. F., JIA, Y. L., ZHANG, F. X., YANG, X. T. & NIU, X. N. 2012 Dual porosity and dual permeability modeling of horizontal well in naturally fractured reservoir. *Transp. Porous Med.* **92** (1), 213–235.

NIELD, D. A. 1968 Onset of thermohaline convection in a porous medium. *Water Resour. Res.* **4** (3), 553–560.

NIELD, D. A. & BEJAN, A. 2017 *Convection in Porous Media*, 5th edn. Springer.

NIELD, D. A. & KUZNETSOV, A. V. 2006 The onset of convection in a bidisperse porous medium. *Intl J. Heat Mass Transfer* **49** (17–18), 3068–3074.

NIELD, D. A. & SIMMONS, C. T. 2007 A discussion on the effect of heterogeneity on the onset of convection in a porous medium. *Transp. Porous Med.* **68** (3), 413–421.

POSTELNICU, A. & REES, D. A. S. 2003 The onset of Darcy–Brinkman convection in a porous layer using a thermal nonequlibrium model – part I: stress-free boundaries. *Intl J. Energy Res.* **27** (10), 961–973.

PRUESS, K. 1983 Heat transfer in fractured geothermal reservoirs with boiling. *Water Resour. Res.* **19** (1), 201–208.

PRUESS, K. & NARASIMHAN, T. N. 1985 A practical method for modeling fluid and heat flow in fractured porous media. *Soc. Petrol. Engng J.* **25** (1), 14–26.

REES, D. A. S., MAGYARI, E. & KELLER, B. 2005 Vortex instability of the asymptotic dissipation profile in a porous medium. *Transp. Porous Med.* **61** (1), 1–14.

SIMMONS, C. T. 2005 Variable density groundwater flow: from current challenges to future possibilities. *Hydrogeol. J.* **13** (1), 116–119.

SIMMONS, C. T., SHARP, J. M. & NIELD, D. A. 2008 Modes of free convection in fractured low-permeability media. *Water Resour. Res.* **44** (3), W03431.

STRAUGHAN, B. 2009 On the Nield–Kuznetsov theory for convection in bidispersive porous media. *Transp. Porous Med.* **77**, 159–168.

STRAUGHAN, B. 2015 *Convection with Local Thermal Non-equilibrium and Microfluidic Effects*. Springer.

STRAUGHAN, B. 2018 Horizontally isotropic bidispersive thermal convection. *Proc. R. Soc. Lond.* A **474** (2213), 20180018.

STRAUGHAN, B. 2019 Horizontally isotropic double porosity convection. *Proc. R. Soc. Lond.* A **475** (2221), 20180672.

VUJEVIĆ, K. & GRAF, T. 2015 Combined inter- and intra-fracture free convection in fracture networks embedded in a low-permeability matrix. *Adv. Water Resour.* **84**, 52–63.

VUJEVIĆ, K., GRAF, T., SIMMONS, C. T. & WERNER, A. D. 2014 Impact of fracture network geometry on free convective flow patterns. *Adv. Water Resour.* **71**, 65–80.

WALKER, K. & HOMSY, G. M. 1977 A note on convective instabilities in Boussinesq fluids and porous media. *J. Heat Transfer* **99** (2), 338–339.

WARREN, J. E. & ROOT, P. J. 1963 The behavior of naturally fractured reservoirs. *Soc. Petrol. Engng J.* **3** (3), 245–255.

WEIS, P. 2015 The dynamic interplay between saline fluid flow and rock permeability in magmatic-hydrothermal systems. *Geofluids* **15**, 350–371.

YANG, J., LATYCHEV, K. & EDWARDS, R. N. 1998 Numerical computation of hydrothermal fluid circulation in fractured Earth structures. *Geophys. J. Intl* **135** (2), 627–649.